CEDAR-GPP: spatiotemporally upscaled estimates of gross primary productivity incorporating CO_2 fertilization

Yanghui Kang[1,2], Max Gaber[1,3], Maoya Bassiouni[1,2], Xinchen Lu[1,2], Trevor F. Keenan[1,2]

[1] Department of Environmental Science, Policy, and Management, University of California, Berkeley, Berkely, CA 94720, USA

[2] Climate and Ecosystem Sciences Division, Lawrence Berkeley National Laboratory, Berkeley, CA 94720, USA

[3] Department of Geosciences and Natural Resource Management, University of Copenhagen, Copenhagen, 1350, Denmark.

Correspondence: Yanghui Kang (yanghuikang@berkeley.edu)
Trevor Keenan (trevorkeenan@berkeley.edu)

Abstract: Gross primary productivity (GPP) is the largest carbon flux in the Earth system, playing a crucial role in removing atmospheric carbon dioxide and providing carbohydrates needed for ecosystem metabolism. Despite the importance of GPP, however, existing estimates present significant uncertainties and discrepancies. A key issue is the underrepresentation of the CO_2 fertilization effect, a major factor contributing to the increased terrestrial carbon sink over recent decades. This omission could potentially bias our understanding of ecosystem responses to climate change.

Here, we introduce CEDAR-GPP, the first global machine-learning-upscaled GPP product that incorporates the direct CO_2 fertilization effect on photosynthesis. Our product is comprised of monthly GPP estimates and their uncertainty at 0.05º resolution from 1982 to 2020, generated using a comprehensive set of eddy covariance measurements, multi-source satellite observations, climate variables, and machine learning models. Importantly, we used both theoretical and data-driven approaches to incorporate the direct CO_2 effects. Our machine learning models effectively predicted monthly GPP ($R^2 \sim 0.74$), the mean seasonal cycles ($R^2 \sim 0.79$), and spatial variabilities ($R^2 \sim 0.67$). Incorporation of the direct CO_2 effects substantially enhanced the predicted long-term trend in GPP across global flux towers by up to 51%, aligning much closer to a strong positive trend from eddy

1

29   covariance data . While the global patterns of annual mean GPP, seasonality, and interannual

30   variability generally aligned with existing satellite-based products, CEDAR-GPP demonstrated

31   higher long-term trends globally after incorporating CO_2 fertilization, particularly in the tropics,

32   reflecting a strong temperature control on direct CO_2 effects. CEDAR-GPP offers a comprehensive

33   representation of GPP temporal and spatial dynamics, providing valuable insights into ecosystem-

34   climate interactions. The CEDAR-GPP product is available at

35   https://zenodo.org/doi/10.5281/zenodo.8212706 (Kang et al., 2024).

36

1. Introduction

Terrestrial ecosystem photosynthesis, known as Gross Primary Productivity (GPP), is the primary source of food and energy for the Earth system and human society (Keenan and Williams, 2018). Through photosynthesis, terrestrial ecosystems also mitigate climate change, by removing thirty percent of anthropogenic carbon emissions from the atmosphere each year (Friedlingstein et al., 2023). However, due to the lack of direct measurements at the global scale, our understanding of photosynthesis and its spatiotemporal dynamics is limited, leading to considerable disagreements among various GPP estimates (Anav et al., 2015; Smith et al., 2016; O'Sullivan et al., 2020; Yang et al., 2022). Addressing these uncertainties is crucial for improving the predictability of ecosystem dynamics under climate change (Friedlingstein et al., 2014).

Over the past three decades, global networks of eddy covariance flux towers collected *in situ* carbon flux measurements that allow for accurate estimates of GPP, providing valuable insights into photosynthesis dynamics under various environmental conditions (Baldocchi, 2020; Beer et al., 2010). To quantify and understand GPP at scales and locations beyond the ~ 1km² flux tower footprints, machine learning has been employed with gridded satellite and climate datasets to upscale site-based measurements and produce wall-to-wall GPP maps (Yang et al., 2007; Xiao et al., 2008; Jung et al., 2011; Tramontana et al., 2016; Joiner and Yoshida, 2020; Zeng et al., 2020; Dannenberg et al., 2023). This "upscaling" approach provides data-driven and observation-based quantifications without prescribed functional relations between GPP and its climatic or environmental drivers. It offers unique empirical constraints of ecosystem carbon dynamics, complementing those derived from process-based and semi-process-based approaches such as terrestrial biosphere models or the Light Use Efficiency (LUE) models (Beer et al., 2010; Jung et al., 2017; Schwalm et al., 2017; Gampe et al., 2021). In recent years, the growth of global and regional flux networks, coupled with increasing efforts in data standardization, has offered new opportunities for the advancement of upscaling frameworks, enabling comprehensive quantifications of terrestrial photosynthesis (Joiner and Yoshida, 2020; Pastorello et al., 2020).

Effective machine learning upscaling depends on a complete set of input predictors that fully explain GPP dynamics. Upscaled datasets have primarily relied on satellite-observed greenness indicators, such as vegetation indices, Leaf Area Index (LAI), the fraction of absorbed photosynthetically active radiation (fAPAR), which effectively capture canopy-level GPP dynamics related to leaf area changes (Tramontana et al., 2016; Ryu et al., 2019; Joiner and Yoshida, 2020).

68 However, important aspects of leaf-level physiology, such as those controlled by climate factors, are

69 often omitted in major upscaled datasets, preventing accurate characterization of GPP responses to

70 climate change (Stocker et al., 2019; Bloomfield et al., 2023). In particular, none of the previous

71 upscaled datasets have considered the direct effect of atmospheric CO_2 on leaf-level photosynthesis,

72 which is a key factor contributing to at least half of the enhanced land carbon sink observed over the

73 past decades (Keenan et al., 2016, 2023; Walker et al., 2021; Ruehr et al., 2023). This omission can

74 lead to incorrect inferences regarding long-term trends in various components of the terrestrial

75 carbon cycle (De Kauwe et al., 2016).

76   Multiple independent lines of evidence from the atmospheric inversion (Wenzel et al., 2016),

77 atmospheric $^{13}C/^{12}C$ measurements (Keeling et al., 2017), ice core records of carbonyl sulfide

78 (Campbell et al., 2017), glucose isotopomers (Ehlers et al., 2015), as well as free-air CO_2 enrichment

79 experiments (FACE) (Walker et al., 2021), suggest a widespread positive effect of elevated

80 atmospheric CO_2 on GPP from site to global scales. Increasing atmospheric CO_2 *directly* stimulates

81 the biochemical rate or the light use efficiency (LUE) of leaf-level photosynthesis, known as the

82 direct CO_2 fertilization effect (CFE). Enhanced photosynthesis could lead to greater net carbon

83 assimilation, contributing to an increase in total leaf area. This expansion, contributing to a higher

84 light interception, further enhances canopy-level photosynthesis (i.e. GPP), which is referred to as

85 the indirect CFE. The direct CFE has been found to dominate GPP responses to CO_2 compared to

86 the indirect effect, from both theoretical and observational analyses (Haverd et al., 2020; Chen et al.,

87 2022).

88   Satellite-based estimates have shown an increasing global GPP trend in the past few decades

89 largely attributable to CO_2-induced increases in LAI (De Kauwe et al., 2016; Zhu et al., 2016; Chen

90 et al., 2019; Piao et al., 2020). However, previous upscaled GPP datasets, as well as most LUE

91 models such as the MODIS GPP product, have failed to consider the direct CO_2 effects on leaf-

92 level biochemical processes (Jung et al., 2020; Zheng et al., 2020). Consequently, these products

93 likely underestimated the long-term trend of global GPP, leading to large discrepancies when

94 compared to process-based models, which typically consider both direct and indirect CO_2 effects

95 (Anav et al., 2015; De Kauwe et al., 2016; Keenan et al., 2023; O'Sullivan et al., 2020). Notably,

96 recent improvements in LUE models have included the CO_2 response and show improved long-

97 term changes in GPP globally (Zheng et al., 2020), yet, this important mechanism is still missing in

98 GPP products upscaled from *in situ* eddy covariance flux measurements based on machine learning

99 models.

100   To improve the quantification of GPP spatial and temporal dynamics and provide a robust

101   representation of long-term dynamics in global photosynthesis, we developed the CEDAR-GPP[1]

102   data product. CEDAR-GPP was upscaled from global eddy covariance carbon flux measurements

103   using machine learning along with a broad range of multi-source satellite observations and climate

104   variables. In addition to incorporating direct CO_2 fertilization effects on photosynthesis, we also

105   account for indirect effects via greenness indicators and include novel satellite datasets such as solar-

106   induced fluorescence (SIF), Land Surface Temperature (LST) and soil moisture to explain variability

107   under environmental stresses. We provide monthly GPP estimations and associated uncertainties at

108   0.05° resolution derived from ten model setups. These setups differ by the temporal range

109   depending on satellite data availability, the method for incorporating the direct CO_2 fertilization

110   effects, and the partitioning approach used to derive GPP from eddy covariance measurements.

111   Short-term model setups were primarily based on data derived from MODIS satellites generating

112   GPP estimates from 2001 to 2020, while long-term estimates spanned 1982 to 2020 using combined

113   Advanced Very High Resolution Radiometer (AVHRR) and MODIS data. We used two approaches

114   to incorporate the direct CO_2 fertilization effects, including direct prescription with eco-evolutionary

115   theory and machine learning inference from the eddy-covariance data. Additionally, we provided a

116   baseline configuration that did not incorporate the direct CO_2 effects. Uncertainties in GPP

117   estimation were quantified using bootstrapped model ensembles. We evaluated the machine learning

118   models' skills in predicting monthly GPP, seasonality, interannual variability, and trend against eddy

119   covariance measurements, and compared the CEDAR-GPP spatial and temporal variability to

120   existing satellite-based GPP estimates.

2. Data and Methods

121

2.1 Eddy covariance data

122

123   We obtained monthly eddy covariance GPP measurements from 2001 to 2020 from the

124   FLUXNET2015 (Pastorello et al., 2020), AmeriFlux FLUXNET

125   (https://ameriflux.lbl.gov/data/flux-data-products/), and ICOS Warm Winter 2020 (Warm Winter

126   2020 Team, 2022) datasets. All data were processed with the ONEFLUX pipeline (Pastorello et al.,

127   2020). Following previous upscaling efforts (Tramontana et al., 2016), we selected monthly GPP

---

[1] CEDAR stands for upsCaling Ecosystem Dynamics with ARtificial inteligence

128   data with at least 80% of high-quality hourly or half-hourly data for temporal aggregation. We

129   further excluded large negative GPP values, setting a cutoff of -1 $gCm^{-2}d^{-1}$. We utilized GPP

130   estimates from both the night-time (GPP_REF_NT_VUT) and day-time (GPP_REF_DT_VUT)

131   partitioning approaches. We classified flux tower sites according to the C3 and C4 plant categories

132   reported in metadata and related publications when available and used a C4 plant percentage map

133   (Still et al., 2003) otherwise. Our analysis encompassed 233 sites, predominately located in North

134   America, Western Europe, and Australia (Figure 1). Despite their uneven geographical distribution,

135   these sites effectively cover a diverse range of climatic conditions and are representative of global

136   biomes (Figure 1c, 1d). In total, our dataset included over 18000 site-months. Note that we did not

137   include eddy covariance data before 2001, since it was limited to only a few sites. This scarcity might

138   introduce biases in the machine learning models, particularly in the relationship between GPP and

139   CO_2, leading to unreliable extrapolations across space and time.
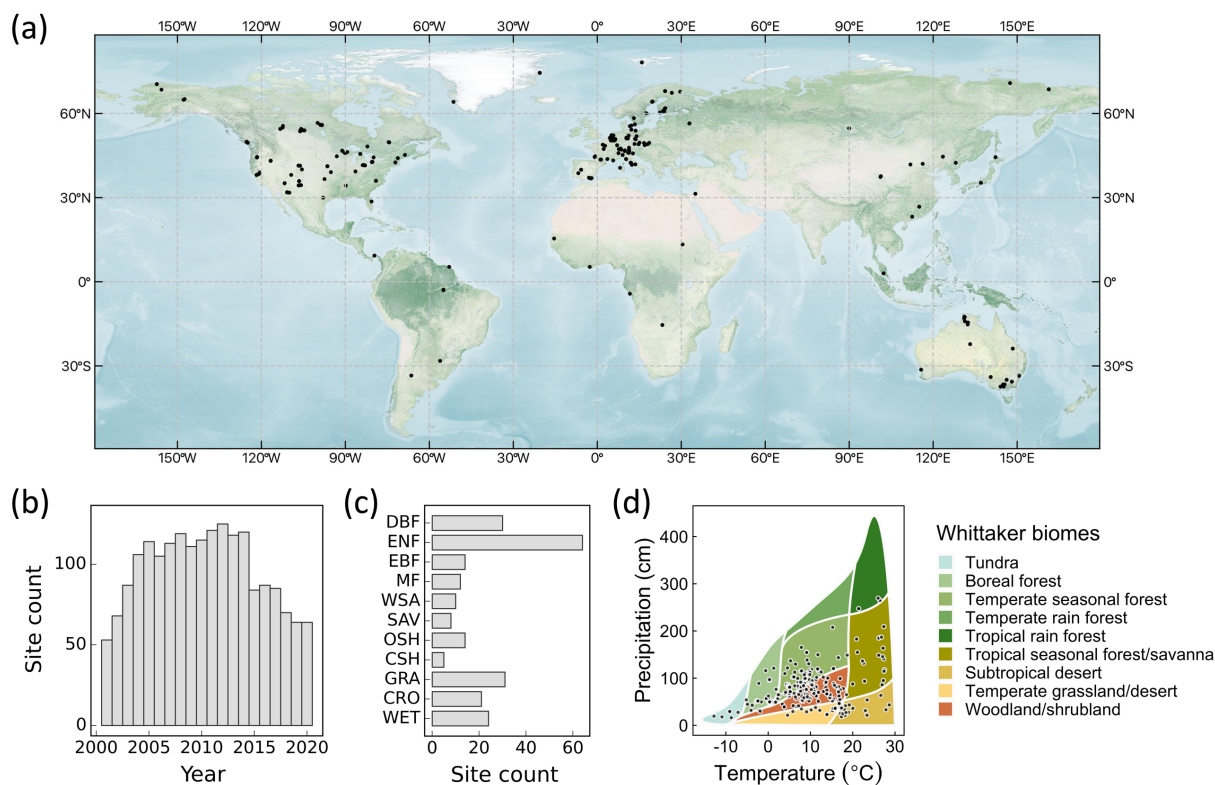
140

141   Figure 1. (a) Spatial distribution of eddy covariance sites used to generate the CEDAR-
142   GPP product. (b) Annual site counts. (c) Site counts by biomes. ENF: evergreen
143   needleleaf forests, EBF: evergreen broadleaf forests, DBF: deciduous broadleaf forests,
144   MF: mixed forests, WSA: woody savannas, SAV: savannas, OSH: open shrublands,
145   CSH: closed shrublands, GRA: grasslands, CRO: croplands, WET: wetlands. (d) Sites

146 distributions in the annual temperature and precipitation space. Whittaker biome
147 classification is shown as a reference of natural vegetation based on long-term climatic
148 conditions. It does not directly indicate the actual biome associated with each site. The
149 base map in (a) was obtained from the NASA Earth Observatory map by Joshua
150 Stevens using data from NASA's MODIS Land Cover, the Shuttle Radar Topography
151 Mission (SRTM), the General Bathymetric Chart of the Oceans (GEBCO), and
152 Natural Earth boundaries. Whittaker biomes were plotted using the "plotbiomes" R
153 package (Ştefan and Levin, 2018).

154 2.2 Global input datasets

155   We compiled an extensive set of covariates from gridded climate reanalysis data, multi-source

156 satellite datasets including optical, thermal, and microwave observations, as well as categorical

157 information on land cover, climate zone, and C3/C4 classification. The datasets that we compiled

158 offer comprehensive information about GPP dynamics and its responses to climatic variabilities and

159 stresses. Table 1 lists the datasets and associated variables used to generate CEDAR-GPP.

160 Table 1. Datasets and input variables used to generate the CEDAR GPP product. For a list of
161 selected variables used in different model setups, please refer to Table S1.

Category	Dataset	Temporal coverage	Spatial resolution	Temporal resolution	Variables	Reference
Climate	ERA5-Land Monthly Averaged data	1950 – present	0.1°	Monthly	Air temperature; vapor pressure deficit, Precipitation, Air and skin temperature, surface downwelling solar radiation, Potential evaporation	(Sabater, 2019)
	ESRA Global Monitoring Laboratory Atmospheric Carbon Dioxide	1976 – present	-	Monthly	Atmospheric CO_2 concentration averaged from Mauna Loa, Hawaii, US and South Pole, Antarctica	(Thoning et al., 2021)
Satellite-based datasets	MODIS Nadir BRDF-adjusted reflectance (MCD43C4v006)	2000 – present	0.05°	Daily	Surface reflectance b1 – b7, Vegetation indices (NIRv, NDVI, kNDVI, EVI, CIgreen, NDWI), percent snow	(Schaaf and Wang, 2015)
	MODIS Terra and Aqua LAI/fPAR (MCD15A3H,	2000 – present	500m	4-day, 8-day	LAI, fPAR	(Myneni et al., 2015a, b)

	MOD15A2H, v006)					
	MODIS Terra and Aqua LST (MYD11A1, MOD11A1, v006)	2000 – present	1 km	Daily	Daytime LST Nighttime LST	(Wan et al., 2015b, a)
	BESS_Rad	2000 – 2020	0.05°	Daily	PAR, diffuse PAR, downwelling solar radiation	(Ryu et al., 2018)
	Continuous-SIF (from OCO-2 and MODIS)	2000 – 2020	0.05°	4-day	all-sky daily average SIF	(Zhang, 2021)
	ESA CCI Soil Moisture Combined Passive and Active (v06.1)	1979 – 2021	0.25°	Daily	Surface soil moisture	(Gruber et al., 2019)
	GIMMS LAI4g	1982 – 2021	0.0833°	Half-month	LAI	(Cao et al., 2023)
	GIMMS NDVI4g	1982 – 2021	0.0833 °	Half-month	NDVI	(Li et al., 2023)
Static categorical datasets	MODIS Land Cover (MCD12Q1v006)	Average status used between 2001 and 2020	500m	-	Plant function types	(Friedl and Sulla-Menashe, 2019)
	Koppen-Geiger Climate Classification	present	1 km	-	Koppen-Geiger climate classes	(Beck et al., 2018)
	C4 percentage map	present	1°	-	Percentage of C4 plants	(Still et al., 2003, 2009)

162

2.2.1 Climate variables

We obtained air temperature, vapor pressure deficit, precipitation, potential evapotranspiration, and skin temperature from the EAR5-Land reanalysis dataset (Sabater, 2019) (Table 1; Table S1). We applied a three-month lag to precipitation, to reflect the memory of soil moisture and represent the root zone water availability. Averaged monthly atmospheric CO_2 concentrations were calculated as an average of records from the Mauna Loa Observatory and South Pole Observation stations, retrieved from NOAA's Earth System Research Laboratory (Thoning et al., 2021).

171   2.2.2   Satellite datasets

172   We assembled a broad collection of satellite-based observations of vegetation greenness and

173   structure, LST, solar radiation, solar-induced fluorescence (SIF), and soil moisture (Table 1, Table

174   S1).

175   We used three MODIS version 6 products: surface reflectance, LAI/fAPAR, and LST.

176   Surface reflectance from optical to infrared bands (band 1 to 7) was sourced from the MODIS

177   Nadir BRDF-adjusted reflectance (NBAR) daily dataset (MCD43C4) (Schaaf and Wang, 2015).

178   From these data, we derived vegetation indices, including NIRv (Badgley et al., 2019), kNDVI

179   (Camps-Valls et al., 2021), NDVI, Enhanced Vegetation Index (EVI), Normalized Difference Water

180   Index (NDWI) (Gao, 1996), and the green chlorophyll index (CIgreen) (Gitelson, 2003). We also

181   used snow percentages from the NBAR dataset. We used the 4-day LAI and fPAR composite

182   derived from Terra and Aqua satellites (MCD15A3H) (Myneni et al., 2015a; Yan et al., 2016a, b)

183   from July 2002 onwards and the MODIS 8-day LAI and fPAR dataset from Terra only

184   (MOD15A2H) prior to July 2002 (Myneni et al., 2015b). We used day-time and night-time LST from

185   the Aqua satellite (MYD11A1) (Wan et al., 2015b), with the Terra-based LST product (MOD11A1)

186   used after July 2002 (Wan et al., 2015a). Terra LST was bias-corrected with the differences in the

187   mean seasonal cycles between Aqua and Terra following Walther et al. (2022).

188   We used the PKU GIMMS NDVI4g dataset (Li et al., 2023) and PKU GIMMS LAI4g (Cao

189   et al., 2023) datasets available from 1982 to 2020. PKU GIMMS NDVI4g is a harmonized time

190   series that includes AVHRR-based NDVI from 1982 to 2003 (with biases and corrections mitigated

191   through inter-calibration with Landsat surface reflectance images) and MODIS NDVI from 2004

192   onward. PKU GIMMS LAI4g consisted of consolidated AVHRR-based LAI from 1982 to 2003

193   (generated using machine learning models trained with Landsat-based LAI data and NDVI4g) and

194   reprocessed MODIS LAI (Yuan et al., 2011) from 2004 onwards.

195   We utilized photosynthetically active radiation (PAR), diffusive PAR, and shortwave

196   downwelling radiation from the BESS_Rad dataset (Ryu et al., 2018). We obtained the continuous-

197   SIF (CSIF) dataset (Zhang et al., 2018; Zhang, 2021) produced by a machine learning algorithm

198   trained using OCO-2 SIF observations and MODIS surface reflectance. We used surface soil

199   moisture from the ESA CCI soil moisture combined passive and active product (version 6.1)

200   (Dorigo et al., 2017; Gruber et al., 2019).

201   2.2.3   Other categorical datasets

202   We used plant functional type (PFT) information derived from the MODIS Land Cover

203   product (MCD12Q1) (Friedl and Sulla-Menashe, 2019). We followed the International Geosphere-

204   Biosphere Program classification scheme but merged several similar categories to maximize the

205   amount of eddy covariance sites/observations available for each category. Closed shrublands and

206   open shrublands are combined into a shrubland category. Woody savannas and savannas are

207   combined into savannas. We generated a static PFT map by taking the mode of the MODIS land

208   cover time series between 2001 – 2020 at each pixel to mitigate uncertainties from misclassification

209   in the MODIS dataset. Nevertheless, changes in vegetation structure induced by land use and land

210   cover change are reflected in the dynamics surface reflectance and LAI/fAPAR datasets we used.

211   We used the Koppen-Geiger main climate groups (tropical, arid, temperate, cold, and polar) (Beck et

212   al., 2018). We also utilized a C4 plant percentage map to account for different photosynthetic

213   pathways when incorporating CO_2 fertilization (Still et al., 2003, 2009). The C4 percentage dataset

214   was constant over time.

215   2.2.4   Data preprocessing

216   We implemented a three-step preprocessing strategy for the satellite datasets: 1) quality

217   control, 2) gap-filling, and 3) spatial and temporal aggregation. In the first step, we selected high-

218   quality data based on the quality control flags of the satellite products when available. For the

219   MODIS NBAR dataset (MCD43C3), we used data with 75% or more high-resolution NBAR pixels

220   retrieved with full inversions for each band. For MODIS LST, we selected the best quality data from

221   the quality control bitmask as well as data where retrieved values had an average emissivity error of

222   no more than 0.02. For MODIS LAI/fAPAR, we used retrievals from the main algorithm with or

223   without saturation. We used all available data in ESA-CCI soil moisture due to the presence of

224   substantial data gaps. In the gap-filling step, missing values in satellite datasets were temporally filled

225   at the native temporal resolution, following a two-step protocol adapted from Walther et al (2021).

226   Short temporal gaps were first filled with medians from a moving window, and the remaining gaps

227   were filled with the mean seasonal cycle. For datasets with a high temporal resolution, including

228   MODIS NBAR (daily), LAI/fPAR (4-day), BESS (4-day), CSIF (4-day), ESA-CCI (daily), temporal

229   gaps no longer than 5 days (8 days for 4-day resolution products) were filled with medians of 15-day

230   moving windows in the first step. An exception is MODIS LST (daily), for which we used a shorter

231   moving window of 9 days due to rapid changes in surface temperature. GIMMS LAI4g and

232 NDVI4g data were only filled with mean seasonal cycle due to their low temporal resolution (half-
233 month). This is because vegetation structure could experience significant changes at half-month
234 intervals, and gap-filling using temporal medians within moving windows could introduce
235 considerable uncertainties and potentially over-smooth the time series. In the last processing step, all
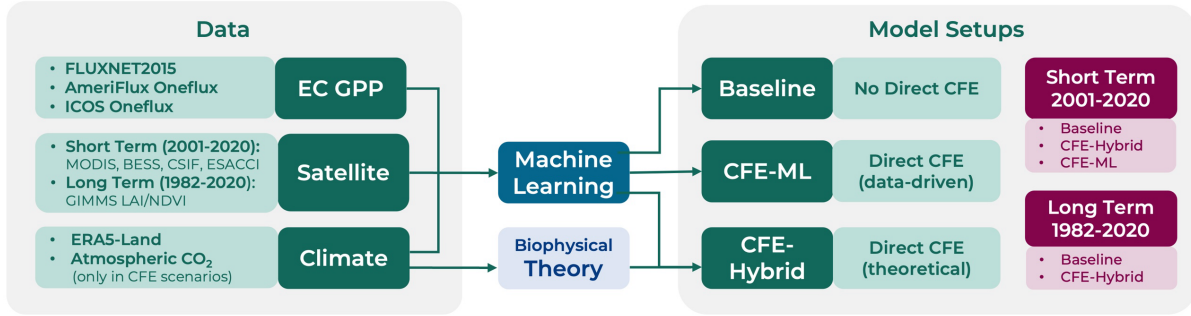236 the datasets were aggregated to a monthly time step and 0.05-degree spatial resolution.

237

238   Figure 2. Schematic overview of the CEDAR-GPP model setups.

2.3   Machine learning upscaling

2.3.1   CEDAR-GPP model setups

241   We trained machine learning models with eddy covariance GPP measurements as targets and
242 climate/satellite variables as input features. We created ten model setups to produce different global
243 monthly GPP estimates (Figure 2; Table 2). The model setups were characterized by the temporal
244 range depending on input data availability, the configuration of CO_2 fertilization effects, and the
245 partitioning approach used to derive the GPP from eddy covariance measurements.
246   The short-term (ST) model configuration produced GPP from 2001 to 2020, and the long-
247 term (LT) configuration spanned 1982 to 2020. Each temporal configuration uses a different set of
248 input variables depending on their availability. Inputs for the short-term configuration included
249 MODIS, CSIF, BESS PAR, ESA-CCI soil moisture, ERA5-Land, as well as PFT and Koppen
250 Climate zone as categorical variables with one-hot encoding. The long-term used GIMMS NDVI4g
251 and LAI4g data, ERA5-land, PFT and Koppen climate. ESA CCI soil moisture datasets were
252 excluded from the long-term model setups due to concerns about the product quality in the early
253 years when the number and quality of microwave satellite data were limited (Dorigo et al., 2015). A
254 detailed list of input features for each setup is provided in Table S1.
255   Regarding the direct (leaf-level) CO_2 fertilization effects (CFE), we established a "Baseline"
256 configuration that did not incorporate these effects, a "CFE-Hybrid" configuration that

11

257 incorporated the effects via eco-evolutionary theory, and a "CFE-ML" configuration that inferred

258 the direct effects from eddy covariance data using machine learning. Detailed information about

259 these approaches is provided in Sec. 2.3.2. Furthermore, separate models were trained for GPP

260 target variables from the night-time (NT) and daytime (DT) partitioning approaches.

261   Table 2 lists the characteristics of ten model setups. Due to the limited availability of eddy

262 covariance observations before 2001, we did not apply the CFE-ML approach to the long-term

263 setups. The CFE-ML model, when trained on data from 2001 to 2020 with atmospheric CO_2

264 ranging from 370 to 412 ppm, would not accurately predict GPP response to CO_2 for the period

265 1982 – 2000 when the CO2 levels were markedly lower (roughly 340 – 369 ppm). This is because

266 machine learning models, especially tree-based models, could not extrapolate beyond the range of

267 the training data.

268 Table 2. Specifications of the CEDAR-GPP model setups.

Model Setup Name	Temporal range	Direct CO_2 Fertilization Effects		GPP Partitioning Method
		Configuration	Method	
ST_Baseline_NT	Short-term (ST)	Baseline	Not incorporated	Night-time (NT)
ST_Baseline_DT	2001 – 2020			Day-time (DT)
ST_CFE-Hybrid_NT		CFE-Hybrid	Theoretical	NT
ST_CFE-Hybrid_DT				DT
ST_CFE-ML_NT		CFE-ML	Data-driven	NT
ST_CFE-ML_DT				DT
LT_Baseline_NT	Long-term (LT)	Baseline	Not incorporated	NT
LT_Baseline_DT	1982 – 2020			DT
LT_CFE-Hybrid_NT		CFE-Hybrid	Theoretical	NT
LT_CFE-Hybrid_DT				DT

269

270 2.3.2 CO_2 fertilization effect

271   We established three configurations regarding the direct CO_2 fertilization effects on

272 photosynthesis. In the baseline configuration, we trained machine learning models with eddy

273 covariance GPP measurements, input climate and satellite features, but excluding CO_2

274 concentration. As such, the models only include indirect CO_2 effects from the satellite-based proxies

275 of vegetation greenness or structure representing changes in canopy light interception, and they do

276 not consider the direct effect of CO_2 on leaf-level photosynthetic rates (or light use efficiency, LUE).

277 Our baseline model is therefore directly comparable to other satellite-derived GPP products that

278 only account for indirect CO2 effects (Jung et al., 2020; Joiner and Yoshida, 2020).

279   In the CFE-ML configuration, we added monthly CO_2 concentration into the feature set in

280   addition to those incorporated in the baseline models. Models inferred the functional relationship

281   between GPP and CO_2 from the eddy covariance data. They, thus encompass both CO_2 fertilization

282   pathways – direct effects on LUE and indirect effects from the satellite-based proxies of vegetation

283   greenness and structure.

284   In the CFE-Hybrid configuration, we applied biophysical theory to estimate the response of

285   LUE to elevated CO_2. First, we estimated a reference GPP, where LUE was not affected by any

286   increase in atmospheric CO_2, by applying the CFE-ML model with a constant atmospheric CO_2

287   concentration equal to the 2001 level while keeping all other variables temporally dynamic. Then, the

288   impacts of CO_2 on LUE were prescribed onto the reference GPP estimates using a theoretical CO_2

289   sensitivity function of LUE according to eco-evolutionary theories (Appendix A). The theoretical

290   CO_2 sensitivity function represents a CO_2 sensitivity that is equivalent to that of the electron-

291   transport-limited (light-limited) photosynthetic rate. When light is limited, elevated CO_2 suppresses

292   photorespiration leading to increased photosynthesis at a lower rate than when photosynthesis is

293   limited by CO_2 (Lloyd and Farquhar, 1996; Smith and Keenan, 2020). Thus, the CFE-Hybrid

294   scenario provides a conservative estimation of the direct CO_2 effects on LUE. Note that the

295   theoretical sensitivity function describes the fractional change in LUE due to direct CO_2 effects

296   relative to a reference period (i.e. 2001). Therefore, we used the CFE-ML model to establish this

297   reference GPP by fixing the CO_2 effects to the 2001 level, rather than simply using the GPP from

298   the Baseline model in which the direct CO_2 effects were not represented.

299   For both CFE-ML and CFE-Hybrid scenarios, we made another conservative assumption that

300   C4 plants do not benefit from elevated CO_2, despite potential increases in photosynthesis during

301   water-limited conditions due to enhanced water use efficiency (Walker et al., 2021). Data from flux

302   tower sites dominated by C4 plants were removed from our training set, so the machine learning

303   models inferred CO_2 fertilization only from flux tower sites dominated by C3 plants. When applying

304   models globally, we assumed the reference GPP values (with constant atmospheric CO_2

305   concentration equal to the 2001 level) to represent C4 plants, and GPP estimates from CFE-ML or

306   CFE-Hybrid models were applied in proportion to the percentage of C3 plants in a grid cell.

307   2.3.3   Machine learning model training and validation

308   We employed the state-of-the-art XGBoost machine learning model, known for its high

309   accuracy in regression problems across various domains, including environmental and ecological

13

310   predictions (Chen and Guestrin, 2016; Kang et al., 2020; Berdugo et al., 2022). XGBoost is a

311   scalable and parallelized implementation of the gradient boosting technique that iteratively trains an

312   ensemble of decision trees, with each iteration targeting to minimize the residuals from the last

313   iteration. A notable merit of XGBoost is its ability to make prediction in the presence of missing

314   values, a common issue in remote sensing datasets. Without relying on prior assumptions about the

315   functional forms or statistical distributions, the model is also robust to multi-collinearity between the

316   predictors in our dataset, particularly for the variables derived from MODIS data.

317   We used five-fold cross-validation for model evaluation. Training data was randomly split into

318   five groups (folds), with each fold held out for testing while the rest four folds were used for model

319   training. We imposed two restrictions on fold splitting: each flux site was entirely assigned to a fold

320   to test model performance over unseen locations; the random sampling was stratified based on PFT

321   to ensure coverage of the full range of PFTs in both training and testing. We also used a nested-

322   cross-validation strategy, during which we performed a randomized search of hyperparameters using

323   three-fold cross-validation within the training set. The nested-cross-validation was aimed to reduce

324   the risk of overfitting and improve the robustness of the evaluation.

325   We assessed the models' ability to capture the temporal and spatial characteristics of GPP,

326   including monthly GPP, mean seasonal cycles, monthly anomalies, and cross-site variability. Model

327   performance was assessed separately for each model setup (Table 2) and summarized by PFT and

328   Koppen climate zone. Mean seasonal cycles were calculated as the mean monthly GPP over the site

329   observation period, and monthly anomalies were the residuals of monthly GPP after subtracting

330   mean seasonal cycles. Monthly GPP averaged over years for each site was used to assess cross-site

331   variability. Goodness-of-fit metrics include RMSE, bias, and coefficient of determination (R^2).

332   To evaluate the models' ability to capture long-term GPP trends, we aggregated the monthly

333   GPP to annual values for sites with at least five years of observations following Chen et al. (2022).

334   GPP anomalies were computed by subtracting the multi-year mean GPP from the annual GPP for

335   each site. Anomalies were aggregated across sites to achieve a single multi-site GPP anomaly per

336   year. We excluded a site-year if less than 11 months of data was available and used linear

337   interpolation to fill the remaining temporal gaps. We used the Sen slope and Mann-Kendall test to

338   examine the GPP trends from 2002 to 2019, excluding 2001 and 2020, due to the limited number of

339   available sites with more than five years of data. We further assessed the aggregated annual trend by

340   grouping the sites based on plant functional types and the koppen climate zones. Categories with

14

341 less than six long-term sites available were excluded from the analysis, which includes EBF and

342 Tropics.

343 2.3.4 Product generation and uncertainty quantification

344 In the CEDAR-GPP product, we generated GPP estimates from each of the ten model

345 setups, by applying the model to global gridded datasets within the corresponding temporal range

346 (Table 2). GPP estimates were named after the corresponding model setups. We used bootstrapping

347 to quantify estimate uncertainties. For each model setup, we generated 30 bootstrapped sample sets

348 of eddy covariance data, which were then used to train an ensemble of 30 XGBoost models. The

349 bootstrapping was performed at the site level, and each bootstrapped sample set contained around

350 140 to 150 unique sites, 17000 to 19000 site months covering all PFTs. The relative PFT

351 composition in the bootstrapped sample sites was consistent with the full dataset. The 30 models

352 trained with bootstrapped samples generated an ensemble of 30 GPP values. We provided the

353 ensemble GPP mean and used standard deviation to indicate uncertainties, for each of the ten model

354 setups.

355 2.4 Product inter-comparison

356 We compared the global spatial and temporal patterns of CEDAR-GPP with other major

357 satellite-based GPP products, including three machine learning upscaled and two LUE-based

358 datasets. We obtained two FLUXCOM products (Jung et al., 2020), the latest version of

359 FLUXCOM-RS (FLUXCOM-RSv006) available from 2001 to 2020 based on remote sensing

360 (MODIS collection 6) datasets only, as well as the FLUXCOM-RS+METEO ensemble available

361 between 1979 to 2018 and based on the climatology of remote sensing observations and ERA5

362 forcings (hereafter FLUXCOM-ERA5). We used FluxSat (Joiner and Yoshida, 2020), available from

363 2001 to 2019, which is an upscaled dataset based on MODIS NBAR surface reflectance and PAR

364 from Modern-Era Retrospective analysis for Research and Applications 2 (MERRA-2). Importantly,

365 FluxSat does not incorporate climate forcings. We used the MODIS GPP product (MOD17)

366 available since 2001, which was generated based on MODIS fAPAR and LUE as a function of air

367 temperature and vapor pressure deficit but not atmospheric CO_2 concentration (Running et al.,

368 2015). We also used the rEC-LUE products, available from 1982 to 2018 and based on a revised

369 LUE model that incorporated the effect of atmospheric CO_2 concentration and the fraction of

370 diffuse PAR on LUE (Zheng et al., 2020). All datasets were resampled to 0.1 ° spatial resolution, and

371 a common mask for the vegetated land area was applied. We evaluated global mean annual GPP,

372 mean seasonal cycle, interannual variability, and trend among different datasets, comparing them

373 over a common time period determined by their data availability. Global total GPP was computed

374 by scaling the global average GPP flux with the global land area (122.4 million km2) following Jung

375 et al. (2020). Mean seasonal cycle was defined as above (Sec. 2.3.3). We used the standard deviation

376 of annual GPP to indicate the magnitude of interannual variability, the Sen slope to indicate the

377 GPP annual trend, and the Mann-Kendall test for the statistical significance of trends.

378 # 3. Results

379 ## 3.1 Evaluation of model performance

380 ### 3.1.1 Overall performance

381 The short-term and long-term models explained approximately 74% and 68%, respectively, of

382 the variation in monthly GPP across global eddy covariance sites (Figure 3a). The long-term models

383 consistently yielded lower performance than the short-term models, likely due to differences in the

384 satellite remote sensing datasets used, as the short-term models benefited from richer information

385 from surface reflectance of individual bands, LST, CSIF, as well as soil moisture, while the long-

386 term model only exploited NDVI and LAI. The models with different CFE configurations and

387 target GPP variables (i.e. partitioning approaches) had similar performance in predicting monthly

388 GPP (Figure 3b, Table S2). All models exhibited minimal bias of less than 0.15.

389 Model performance in terms of the different temporal and spatial characteristics of monthly

390 GPP was variable (Figure 3c-h). The models were most successful at predicting mean seasonal

391 cycles, with the short-term and long-term models explaining around 79% and 73% of the variability,

392 respectively (Figure 3c-d). The short-term and long-term models captured 67% and 56% ,

393 respectively, of the spatial variabilities in multi-year mean GPP across global sites (i.e., cross-site

394 variability) (Figure 3g-h). However, all models underestimated monthly anomalies across the sites,

395 with R^2 values below 0.12 (Figure 3e-f). The CFE-ML and CFE-Hybrid models showed slightly

396 higher accuracy than the Baseline model across all temporal and spatial characteristics in NT setups.

397 Patterns from the DT setups do not significantly differ from those of the NT setups (Figure S1).
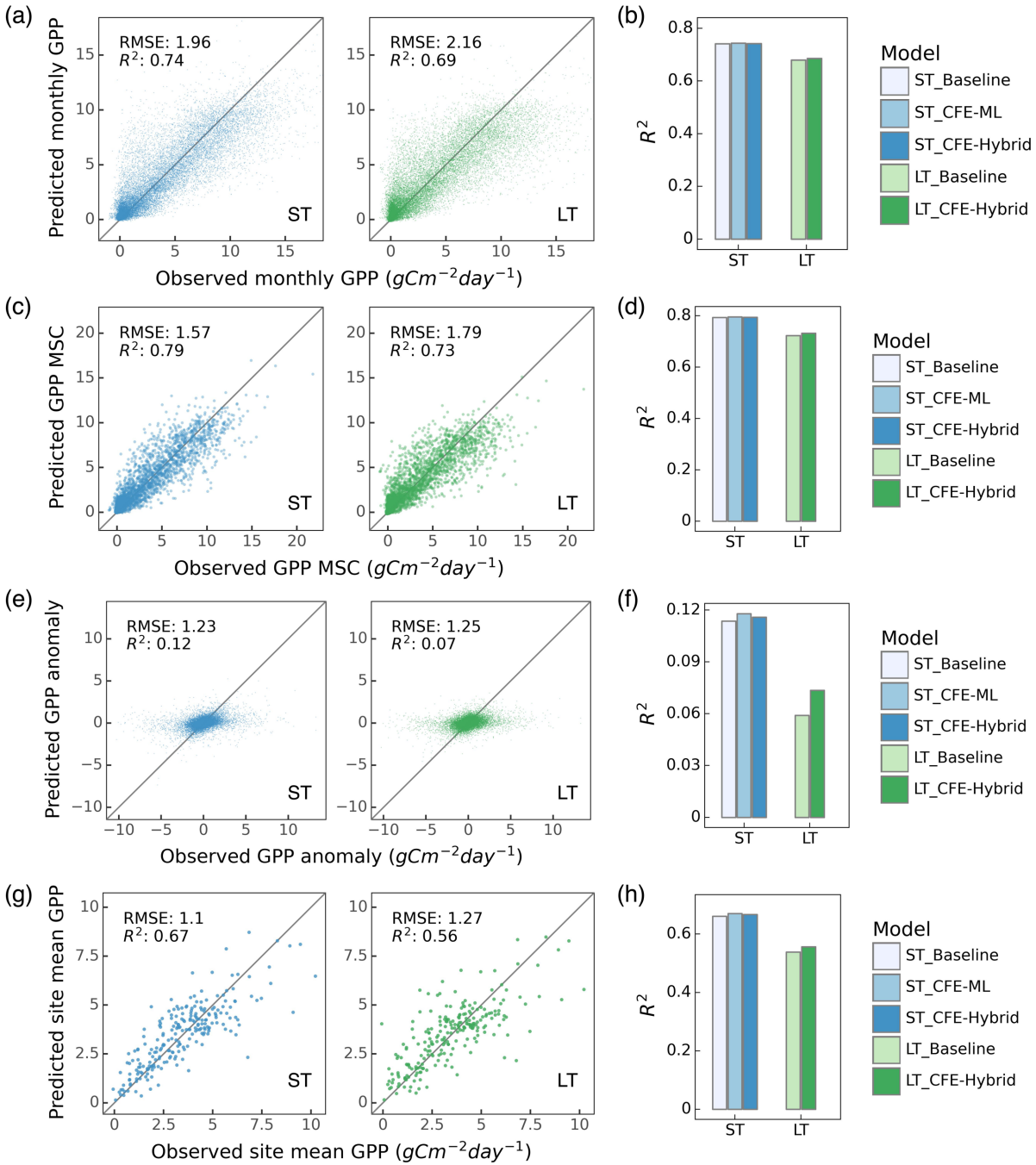
398

16

Figure 3. Machine learning model performance in predicting monthly GPP and its spatial and temporal variability. Only NT models are shown and DT results is provided in Supplementary Figure S1. Scatter plots illustrated relationships between model predictions and observations for monthly GPP (a), mean seasonal cycles (MSC) (c), monthly anomaly (e), and cross-site variability (g) for ST_CFE-Hybrid_NT (left, blue) and LT_CFE-Hybrid_NT (right, green) models. Corresponding bar plots show the R^2 values for five NT model setups in predicting monthly GPP (b), MSC (d), monthly anomaly (f), and cross-site variability (h).

408   3.1.2   Performance by biome and climate zone

409   The predictive ability of our models varied across different PFTs and Koppen climate zones

410   (Figure 4). Here we present results from the CFE-Hybrid LT and ST models based on NT

411   partitioning and note that patterns for the other CFE configurations and the DT GPP were similar

412   (Figure S2).

413   Model performance in terms of monthly GPP was the highest for deciduous broadleaf forests,

414   mixed forests, and evergreen needleleaf forests, with R^2 values above 0.78. Model accuracies were

415   also high for savannas and grasslands, followed by croplands and wetlands, with R^2 values between

416   0.57 and 0.74. Model accuracies were lowest in evergreen broadleaf forests and shrublands, with R^2

417   values as low as 0.14. Across climate zones, models achieved the highest accuracy in predicting

418   monthly GPP in cold and tropical climate zones with R^2 values between 0.64 and 0.80. The short-

419   term models had the lowest performance in polar regions with an R^2 value of around 0.42, and the

420   long-term model had the lowest performance in arid regions with an R^2 value of 0.25.

421   Model performance in terms of mean seasonal cycles across PFTs and climate zones followed

422   patterns for monthly GPP, while disparities emerged for performance in terms of GPP anomaly and

423   cross-site variability (Figure 4). The short-term model showed the highest predictive power in

424   explaining monthly anomalies in arid regions with an R^2 value of 0.49, where savanna and

425   shrublands sites are primarily located. Model performance in all other climate zones was significantly

426   lower, with R^2 values below 0.2, and as low as 0.07 in temperate regions. Besides, the short-term

427   model demonstrated good performance in capturing anomalies in deciduous broadleaf forests. The

428   long-term model's relative performance between PFTs and climate zones was mostly consistent with

429   that of the short-term model, with lower accuracy in shrublands when compared to the short-term

430   model.

431   Models demonstrated the highest accuracy in predicting cross-site variability in savannas,

432   grasslands, evergreen needleleaf forests, and evergreen broadleaf forests ($R^2 > 0.36$) and the lowest

433   accuracy in deciduous broadleaf forests, mixed forests, and croplands ($R^2 < 0.20$). The short-term

434   model additionally showed good performance in shrublands and wetlands ($R^2 > 0.36$), whereas the

435   long-term model failed to capture any variability for shrublands. In terms of climate zones, models

436   were most successful at explaining the variabilities within tropical and cold climate zones ($R^2 >$

437   0.46), the short-term model was least successful across polar regions, with a R^2 value of 0.29, and the

438   long-term model had low performance for both polar and arid regions with R^2 values below 0.15.
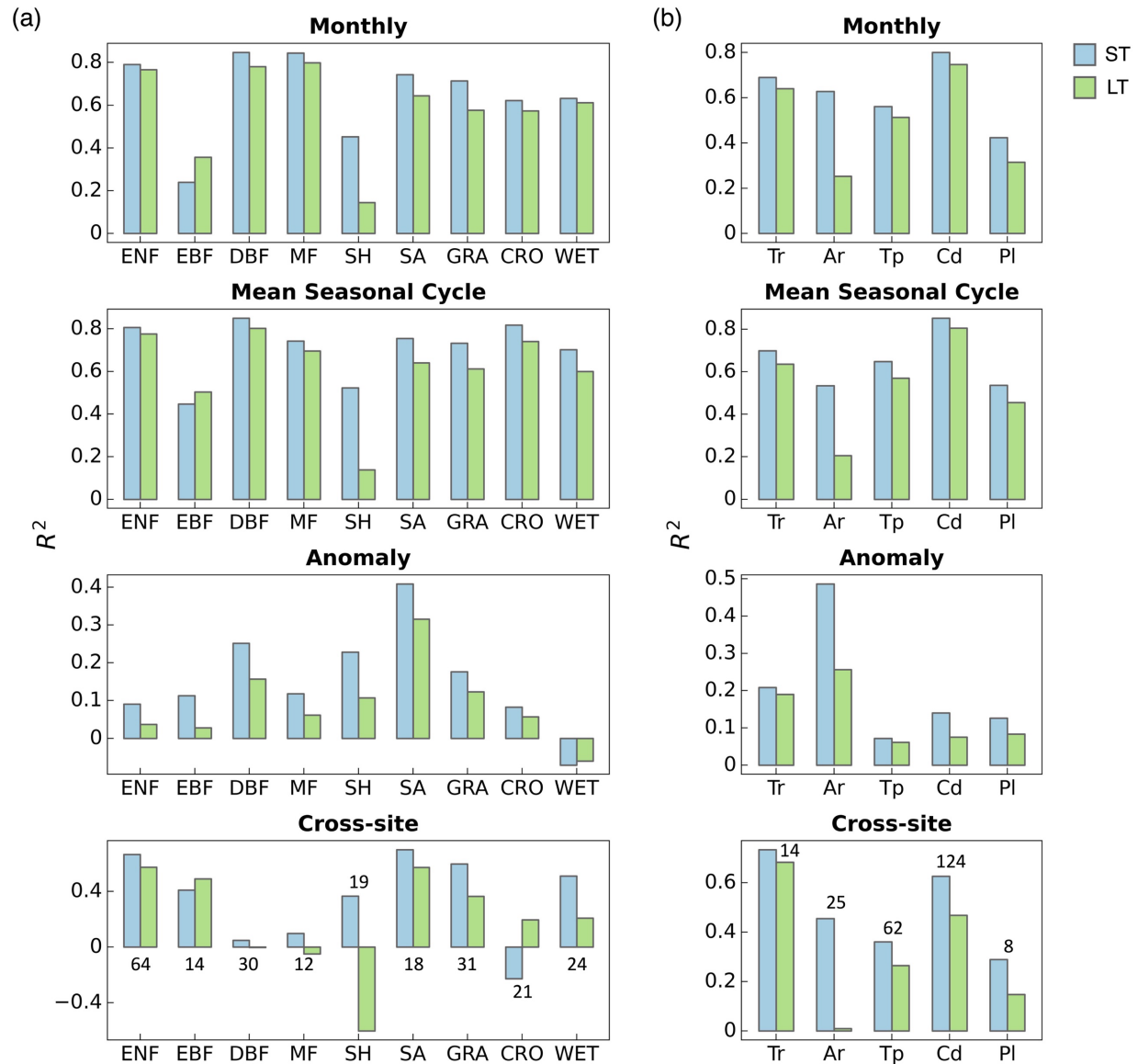
18

Figure 4. Performance of the ST_CFE-Hybrid_NT (blue) and LT_CFE-Hybrid_NT (green) models on GPP spatiotemporal estimation by plant functional types (a) and climate zones (b). The cross-site panels included the number of sites within each category. Color indicates short-term (ST) or long-term (LT) models. ENF: evergreen needleleaf forest, EBF: evergreen broadleaf forest, DBF: deciduous broadleaf forest, MF: mixed forest, SH: shrubland, SA: savanna, GRA: grassland, CRO: cropland, WET: wetland. Tr: tropical, Ar: arid, Tp: temperate, Cd: cold, Pl: polar. The performance of DT models is displayed in Supplementary Figure S2.

3.1.3   Prediction of long-term trends

Eddy covariance derived GPP presented a substantial increasing trend across flux sites between 2002 and 2019 (Figure 5a, Figure S3a). The observed GPP from the night-time partitioning

19

451   approach indicated an overall trend of 7.7 $gCm^{-2}year^{-2}$. In contrast, the ST_ Baseline_NT model

452   predicted a more modest trend of 2.7 $gCm^{-2}year^{-2}$, primarily reflecting the indirect CO_2 effect

453   manifested through the growth of LAI. Both the ST_CFE-ML_NT and ST_CFE-hybrid_NT

454   models predicted much higher trends of 5.5 and 4.3 $gCm^{-2}year^{-2}$ respectively, representing an

455   improvement from the Baseline model by 51% and 29%, aligning more closely to eddy covariance

456   observations. Similarly the LT_CFE-Hybrid_NT model showed an improved trend estimation than

457   the LT_Baseline_NT model. All trends were statistically significant ($p < 0.05$).

458   Aggregated eddy covariance GPP experienced increasing trends of varied magnitudes across

459   different climate zones and plant functional types (Figure 5b,c; Figure S3b,c). While the machine

460   learning models generally did not fully capture the enhancement in GPP for most categories, the

461   CFE-ML and/or CFE-hybrid models consistently outperformed the Baseline models in both ST

462   and LT setups. The CFE-ML setup predicted a higher trend than CFE-hybrid in most cases,

463   suggesting that the data-driven approach captured more dynamics not represented in the theoretical

464   model, which was based on conservative assumptions regarding the CO_2 sensitivity of

465   photosynthesis (see Sect. 2.3.2 and Appendix A). The choice of remote sensing data (ST vs. LT

466   configurations) did not lead to substantial differences in the predicted GPP trend. Most long-term

467   flux sites (at least 10 years of records) with a significant trend experienced an increase in GPP, and

468   the CFE-ML and/or CFE-hybrid models aligned closer to eddy covariance data than the Baseline

469   models (Figure S4). Additionally, we found a considerably higher trend in eddy covariance GPP

470   measurements derived from the day-time versus night-time partitioning approach, potentially

471   associated with uncertainties in GPP partitioning methods (Figure S4). Yet, machine learning model

472   predicted trends were not strongly affected by GPP partitioning methods (Figure S3, S4).
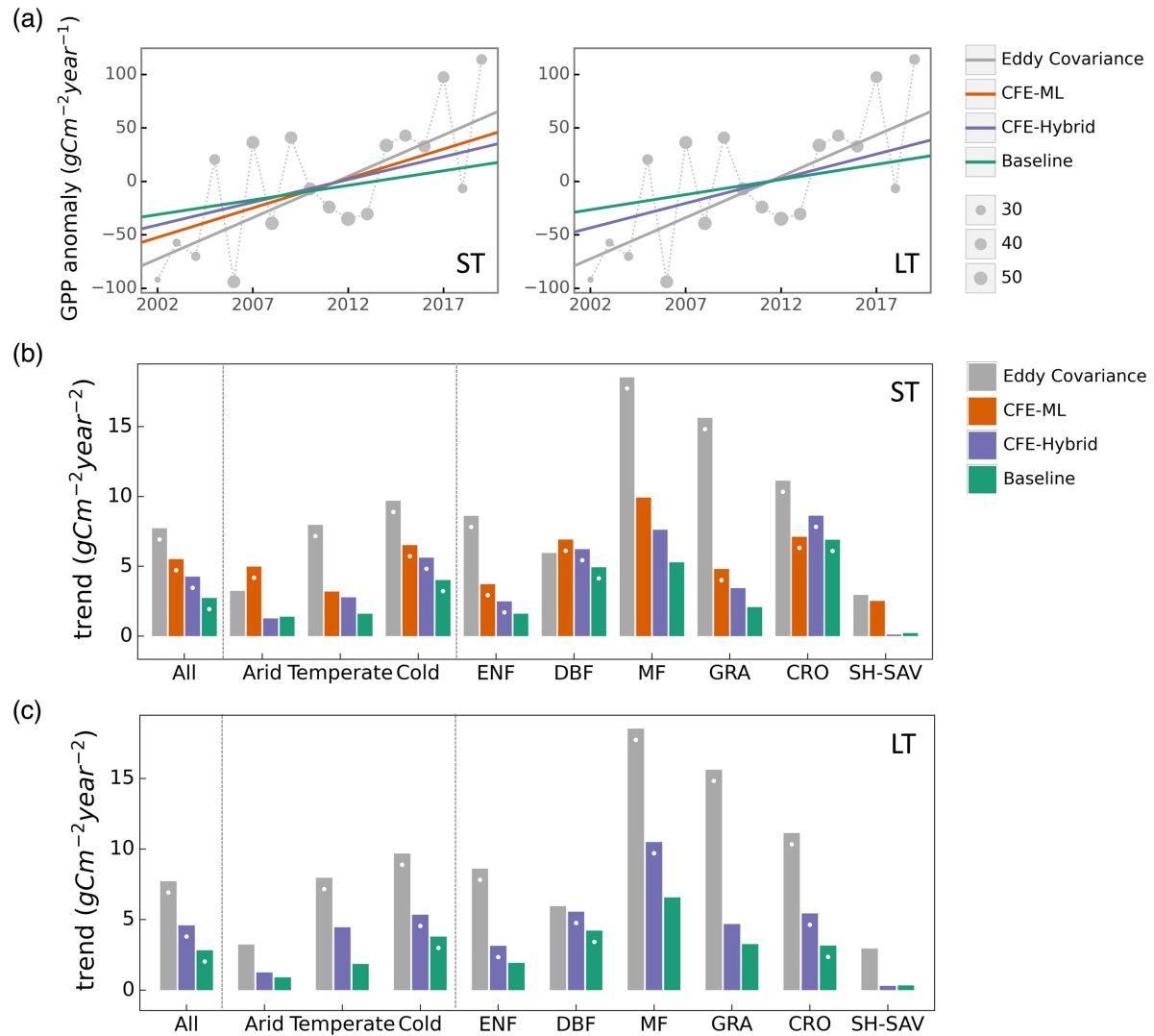
473

Figure 5. Comparison of observed and predicted GPP (from NT models only) trends across eddy covariance flux towers. (a) Aggregated annual GPP anomaly from 2002 to 2019 and trend lines from eddy covariance (EC) measurements, and three CFE model setups (short-term, night-time partitioning) for ST (left) and LT (right) models. The size of grey circle markers is proportional to the number of sites. (b) Comparison of annual GPP trends from eddy covariance measurements and the short-term (ST) CEDAR-GPP model setups by plant functional types and climate zones. (c) Comparison of annual GPP trends from eddy covariance measurements and the long-term (LT) CEDAR-GPP model setups by plant functional types and climate zones. In (b) and (c), Categories with less than 6 sites, including Tropics and EBF, were not shown. While dots on the bars indicate statistically significant trend with p-value < 0.1. Results for the DT models are shown in Supplementary Figure S3.

3.2 Evaluation of GPP spatial and temporal dynamics

We compared CEDAR-GPP estimates with other upscaled or LUE-based datasets regarding the mean annual GPP (Sect. 3.2.1), GPP seasonality (Sect. 3.2.2), interannual variability (Sect. 3.2.3), and annual trends (Sect. 3.2.4). CEDAR-GPP model setups generally showed similar patterns in mean annual GPP, seasonality, and interannual variability, therefore, in corresponding sections, we present the CFE-Hybrid model setups as representative examples for comparisons with other datasets, unless otherwise stated. Supplementary figures include comparisons involving CEDAR-GPP estimates from all model setups.

3.2.1 Mean annual GPP

Global patterns of mean annual GPP were generally consistent among CEDAR-GPP model setups, FLUXCOM, FLUXSAT, MODIS, and rEC-LUE, with few noticeable regional differences (Figure 6, Figure S5). Differences among CEDAR-GPP model setups were minimal and only evident between the NT and DT setups in the tropics (Figure 6b-c, Figure S5). CEDAR-GPP short-term datasets showed highest consistency with FLUXSAT in terms of mean annual GPP magnitudes (2001 – 2018) and latitudinal variations, although FLUXSAT presented slightly higher GPP values in the tropics compared to CEDAR-GPP (Figure 6b). Mean annual GPP magnitude for FLUXCOM-RS006 and MODIS was lower globally than CEDAR-GPP and FLUXSAT, with the most pronounced differences observed in the tropical areas. Among the long-term datasets (CEDAR-GPP LT, FLUXCOM-ERA5, and rEC-LUE), mean annual GPP (1982 – 2018) exhibited greater disparities in the northern mid-latitudes than in the tropics and southern hemisphere (Figure 6c). CEDAR-GPP aligned more closely with FLUXCOM-ERA5 than with rEC-LUE, with the latter showing lower annual mean GPP globally, particularly between 20ºN to 50º N.
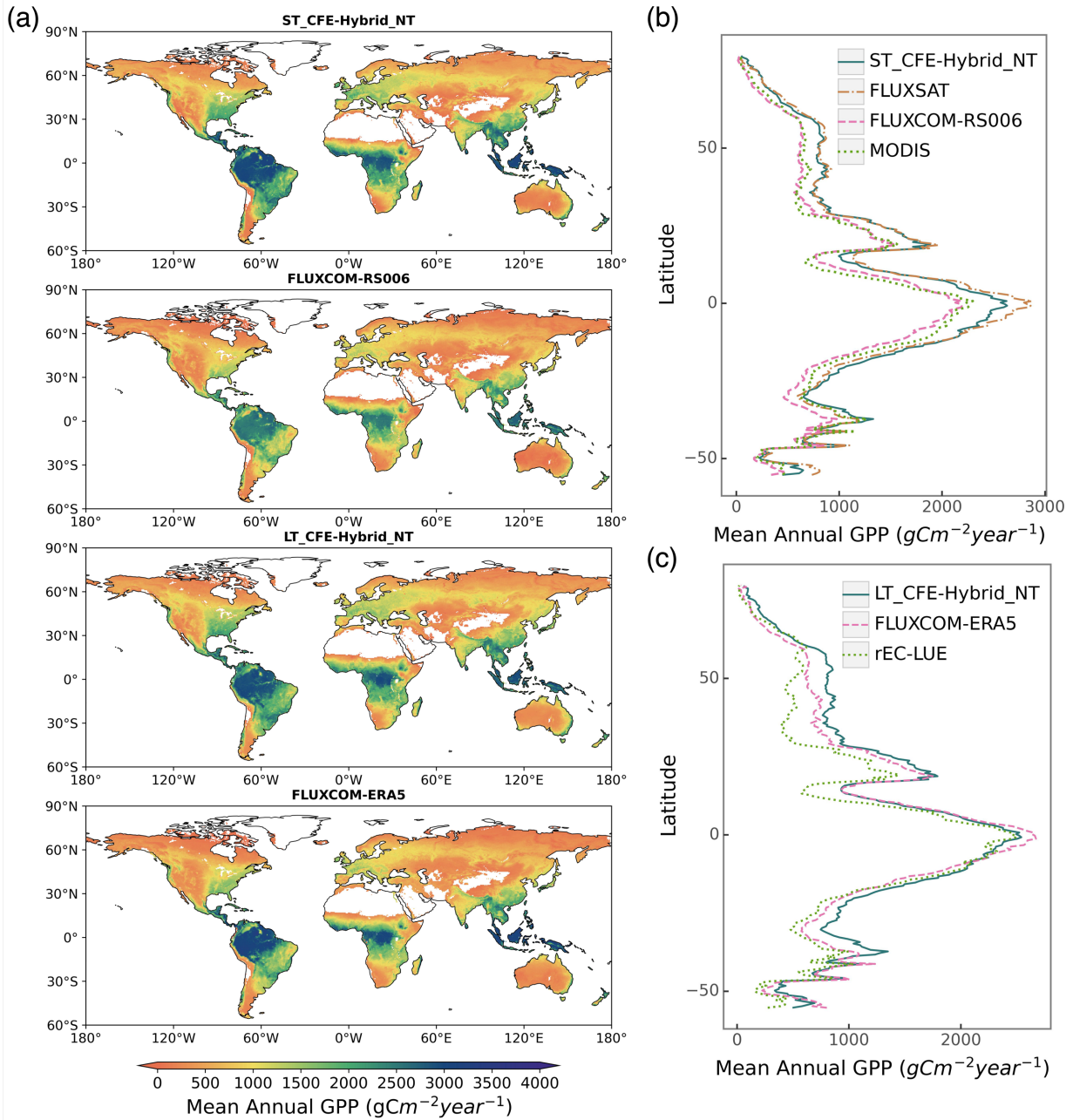
22

Figure 6. Global distributions of mean annual GPP from CEDAR-GPP and other machine learning upscaled and LUE-based reference datasets. (a) Global patterns of mean annual GPP from two short-term datasets including ST_CFE-Hybrid_NT, and FLUXCOM-RS006, and two long-term datasets including LT_CFE-Hybrid_NT, and FLUXCOM-ERA5. (b) Latitudinal distributions of mean annual GPP from short-term datasets (ST_CFE-Hybrid_NT, FLUXSAT, FLUXCOM-RS006, and MODIS). (c) Latitudinal distributions of mean annual GPP from long-term datasets (LT_CFE-Hybrid_NT, FLUXCOM-ERA5, and rEC-LUE). Mean annual GPP was computed between 2001 and 2018 for short-term datasets and between 1982 and 2018 for long-term datasets.

23

521   3.2.2   Seasonal variability

522   CEDAR-GPP and other machine learning upscaled or LUE-based GPP datasets agreed on

523   seasonal variabilities (average between 2001 and 2018) at the global scale, characterized by a peak in

524   GPP in July and a nadir between December and January (Figure 7, Figure S6, S7). At the global

525   scale, CEDAR-GPP was most closely aligned with FLUXSAT in GPP seasonal magnitude and

526   amplitude, while both FLUXCOM and MODIS displayed a relatively less pronounced magnitude.

527   In the northern hemisphere (20ºN - 90ºN), all GPP datasets agreed on seasonal GPP

528   variation, despite variances in the magnitude of peak GPP. In the southern hemisphere (20ºS -

529   60ºS), all datasets exhibited their lowest GPP during June and July, and highest GPP from

530   December to January. However, the seasonal amplitude of GPP was greatest for FLUXCOM-

531   ERA5, followed by CEDAR-GPP and FLUXSAT, and substantially smaller for FLUXCOM-RS006

532   and MODIS GPP. In the tropics (20ºN - 20ºS), differences between datasets were the strongest,

533   where seasonal variation is not as prominent compared to other regions. CEDAR-GPP, FLUXSAT,

534   and FLUXCOM-ERA5 each showed two GPP peaks, occurring in March-April and September-

535   October. Although FLUXCOM-RS006 had a similar seasonal pattern, its GPP magnitude was

536   markedly smaller. Interestingly, MODIS showed an inverse season pattern with a small peak from

537   June to August.
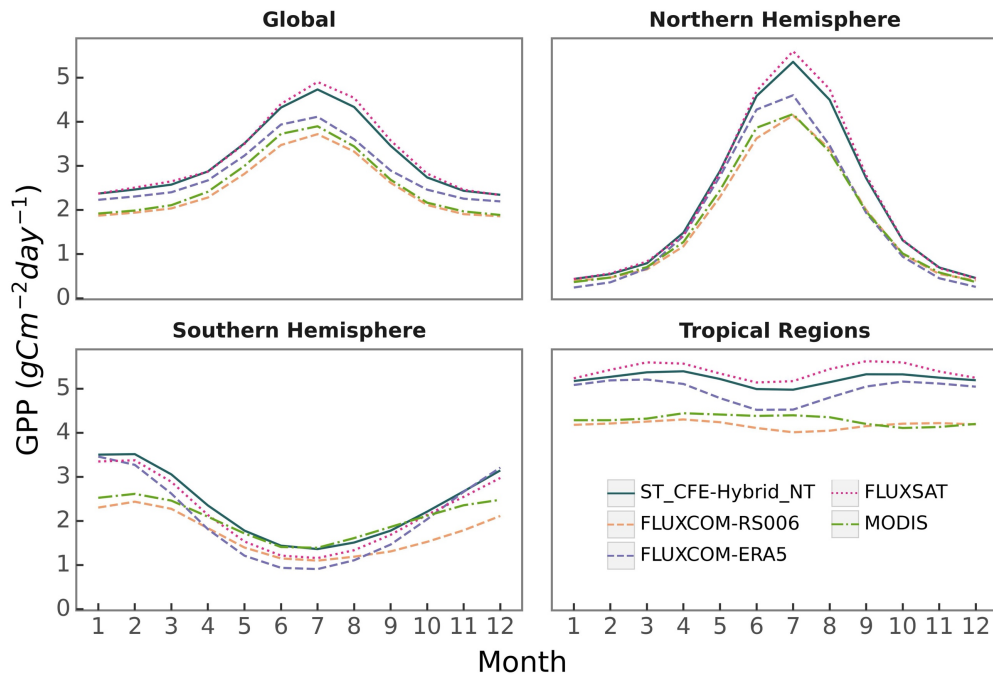
538

539   Figure 7. Comparison of GPP mean seasonal cycle between different datasets on a
540   global scale, specifically within the Northern Hemisphere (20ºN - 90ºN), Southern

541   Hemisphere (20ºS - 60ºS), and Tropical regions (20ºN - 20ºS). Monthly means were
542   averaged from 2001 to 2018 for all datasets.

543   3.2.3   Interannual variability

544   We found distinct spatial patterns in GPP interannual variability between upscaled and LUE-

545   based datasets and a high level of agreement within each category, with the exception of

546   FLUXCOM-ERA5, which showed minimal interannual variability globally (Figure 8, Figure S8). All

547   datasets agreed on the presence of GPP interannual variability hotspots in eastern and southern

548   South America, central North America, southern Africa, and western Australia. These hotspots

549   primarily corresponded to arid and semi-arid areas characterized by grasslands, shrubs, and

550   croplands (Figure 9). CEDAR-GPP was highly consistent with FLUXSAT, and both datasets also

551   displayed relatively high interannual variability in the dry subhumid areas of Europe, predominately

552   covered by croplands. FLUXCOM-RS006 mirrored the relative spatial patterns of CEDAR-GPP

553   and FLUXSAT, albeit at lower magnitudes. The LUE-based datasets (MODIS and rEC-LUE)

554   predicted a much higher interannual variability than the upscaled datasets in the tropical areas,

555   particularly in evergreen broadleaf forests and woody savannas (Figure 8, Figure 9). These datasets

556   also depicted slightly higher interannual variability for other types of forests, including evergreen

557   needleleaf forests and deciduous broadleaf forests, compared to the upscaled datasets. The lack of

558   interannual variability in FLUXCOM-ERA5 is attributable to the use of mean seasonal cycles of

559   remotely sensed vegetation greenness indicators rather than their dynamic time series. Ten CEDAR-

560   GPP model setups presented consistent patterns in interannual variability, and differences were
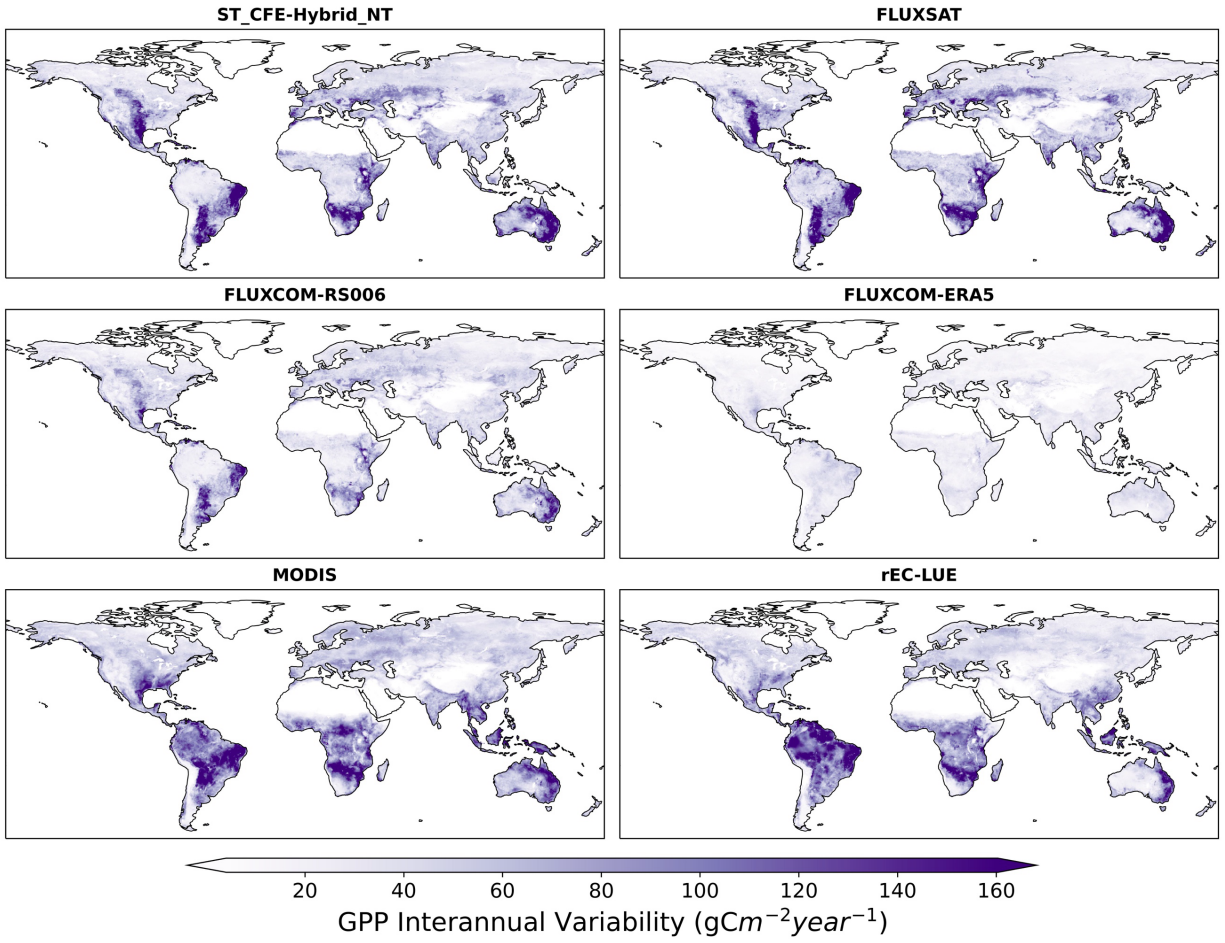
561   minimal (Figure S8).

Figure 8. Spatial patterns of GPP interannual variability extracted over 2001 to 2018 for CEDAR-GPP (ST_CFE-Hybrid_NT), FLUXSAT, FLUXCOM-RS006, MODIS, FLUXCOM-ERA5, and rEC-LUE.
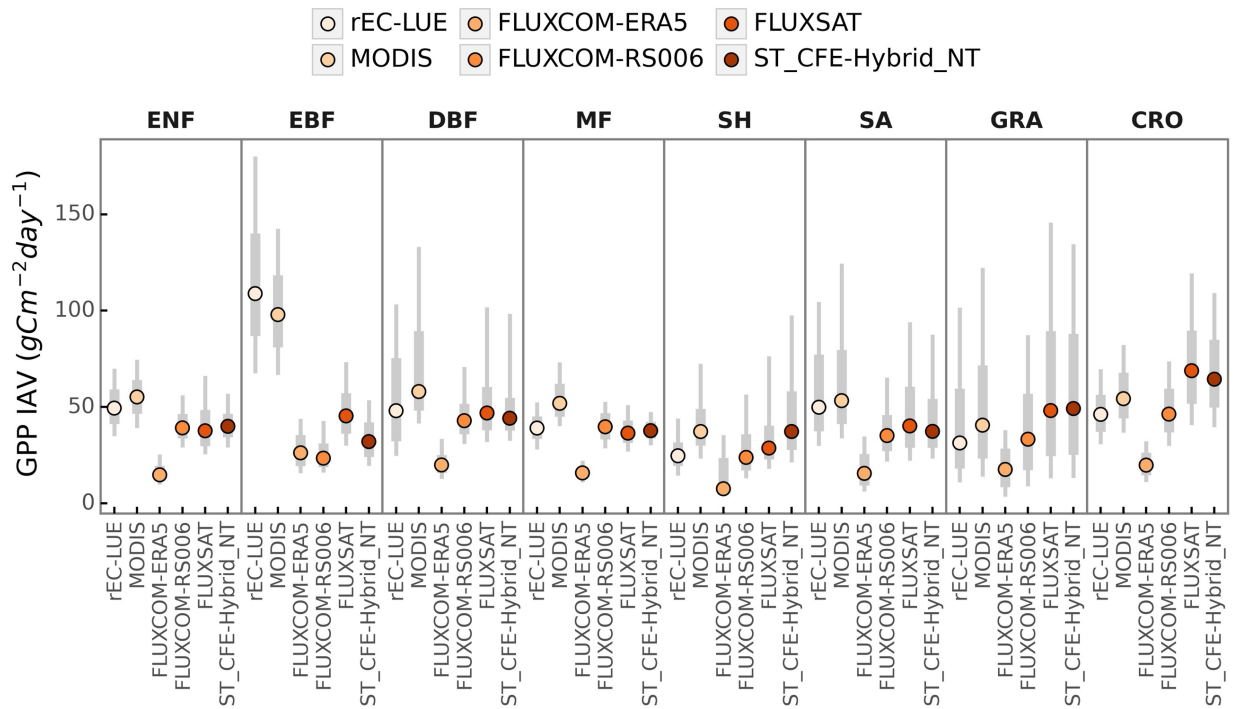
26

Figure 9. Comparison of GPP interannual variability (IAV) across global datasets by PFT. Colored dots represent the median IAV, thicker gray bars indicate the 25% to 75% percentiles of IAV distributions, and thinner grey bards show the 10% to 90% percentiles.

3.2.4 Trends

Differences in annual GPP trends among CEDAR-GPP model setups and other upscaled and LUE-based datasets mainly reflected the variability in the representation of CO_2 fertilization effects (Figure 10, Figure S9). From 2001 to 2018, the CEDAR-GPP Baseline model setups showed spatial variations in GPP trends consistent with the other upscaled datasets without direct CO_2 fertilization effects, including FLUXSAT and FLUXCOM-RSv006. In these datasets, substantial increases were seen in southeastern China and India, western Europe, and part of North and South America. These increases were largely associated with rising LAI due to land use changes and indirect CO_2 fertilization effects, as identified by previous studies (Zhu et al., 2016; Chen et al., 2019). Although MODIS, which also does not include a direct CO_2 fertilization effect, generally agreed with these increasing trends, it also showed a declining GPP in the tropical Amazon and a stronger positive trend in central South America. After incorporating the direct CO_2 fertilization effects, both the CFE-Hybrid and CFE-ML setups predicted positive trends in tropical forests, an observation absent in all other datasets. Furthermore, the CFE-Hybrid and CFE-ML models also revealed increasing

585 GPP in temperate and boreal forests of North America and Eurasia. Notably, all datasets agreed on

586 a pronounced GPP decrease in eastern Brazil.

587   From 2001 to 2018, a positive trend in global annual GPP was uniformly detected by all

588 datasets, albeit with varying magnitudes (Figure 11a-b). The ST_Baseline_NT model predicted a

589 GPP growth rate of 0.35 Pg C per year, aligning with FLUXCOM-RS, but lower than FLUXSAT

590 (0.51 Pg C yr^{-2}) and MODIS (0.39Pg C yr^{-2}) (Figure 11b). The CFE-hybrid models estimated a

591 notably faster GPP growth at 0.58 Pg C yr^{-2}. The CFE-ML models predicted the highest trends, up

592 to 0.76 Pg C yr^{-2} from the ST_CFE-ML_NT model and 0.59 Pg C yr^{-2} from the ST_CFE-ML_DT

593 model. Also, a higher variance was observed among ensemble members in the ST_CFE-ML setups

594 compared to the ST_Baseline and ST_CFE-Hybrid models.

595   The LT_Baseline_NT model identified increasing GPP trends in large areas of Europe, East

596 and South Asia, as well as the Northern Amazon from 1982 to 2020 (Figure 10b). The pattern from

597 the LT_CFE-Hybrid_NT model aligned closely with the LT_Baseline_NT model but exhibited a

598 stronger positive trend in global tropical areas as well as Eurasian boreal forests. In contrast,

599 FLUXCOM-ERA5 showed overall negative trends in the tropics, with a small magnitude. Lastly,

600 rEC-LUE agreed with positive GPP trends identified in CEDAR-GPP in the extratropical areas, but

601 predicted a pronounced negative trend in the tropics. At the global scale, all the CEDAR-GPP long-

602 term models predicted a positive global GPP trend (Figure 11d). The LT_Baseline models showed a

603 trend of 0.13 to 0.15 Pg C yr^{-2}, while the LT_CFE-Hybrid setups doubled that rate. rEC-LUE

604 showed a two-phased pattern with a strong increase in GPP from 1982 to 2000 (0.54 Pg C yr^{-2}),

605 followed by a decreasing trend after 2001 (-0.20 Pg C yr^{-2}) (Figure S10). This resulted in an overall

606 positive change at a rate comparable to that of the Baseline model. FLUXCOM-ERA5 exhibited a

607 small negative trend.

(a)

ST_Baseline_NT   ST_CFE-Hybrid_NT

ST_CFE-ML_NT   FLUXCOM-RS006

FLUXSAT   MODIS

GPP Annual Trend (gC $m^{-2}year^{-2}$)

(b)

LT_Baseline_NT   LT_CFE-Hybrid_NT

FLUXCOM-ERA5   rEC-LUE
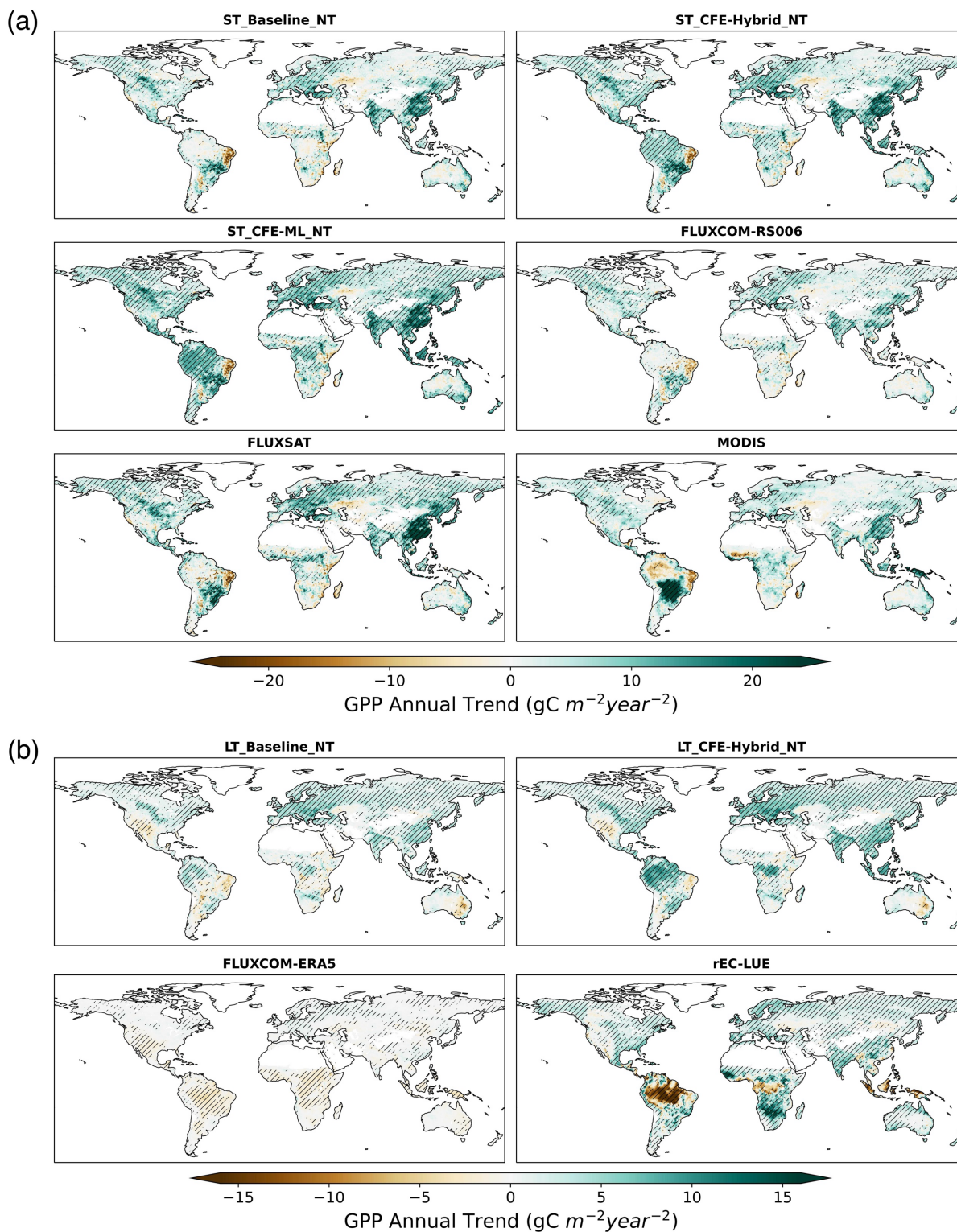
GPP Annual Trend (gC $m^{-2}year^{-2}$)

608

609   Figure 10. Annual GPP trend over 2001 – 2018 for short-term CEDAR-GPP,
610   FLUXCOM-RS006, FLUXSAT, and MODIS datasets (a) and over 1982 – 2018 for
611   long-term CEDAR-GPP, FLUXCOM-ERA5 and rEC-LUE datasets (b). Hatched

29

areas indicate the GPP trend that is statistically significant at p < 0.05 level under the
Mann-Kendal test.
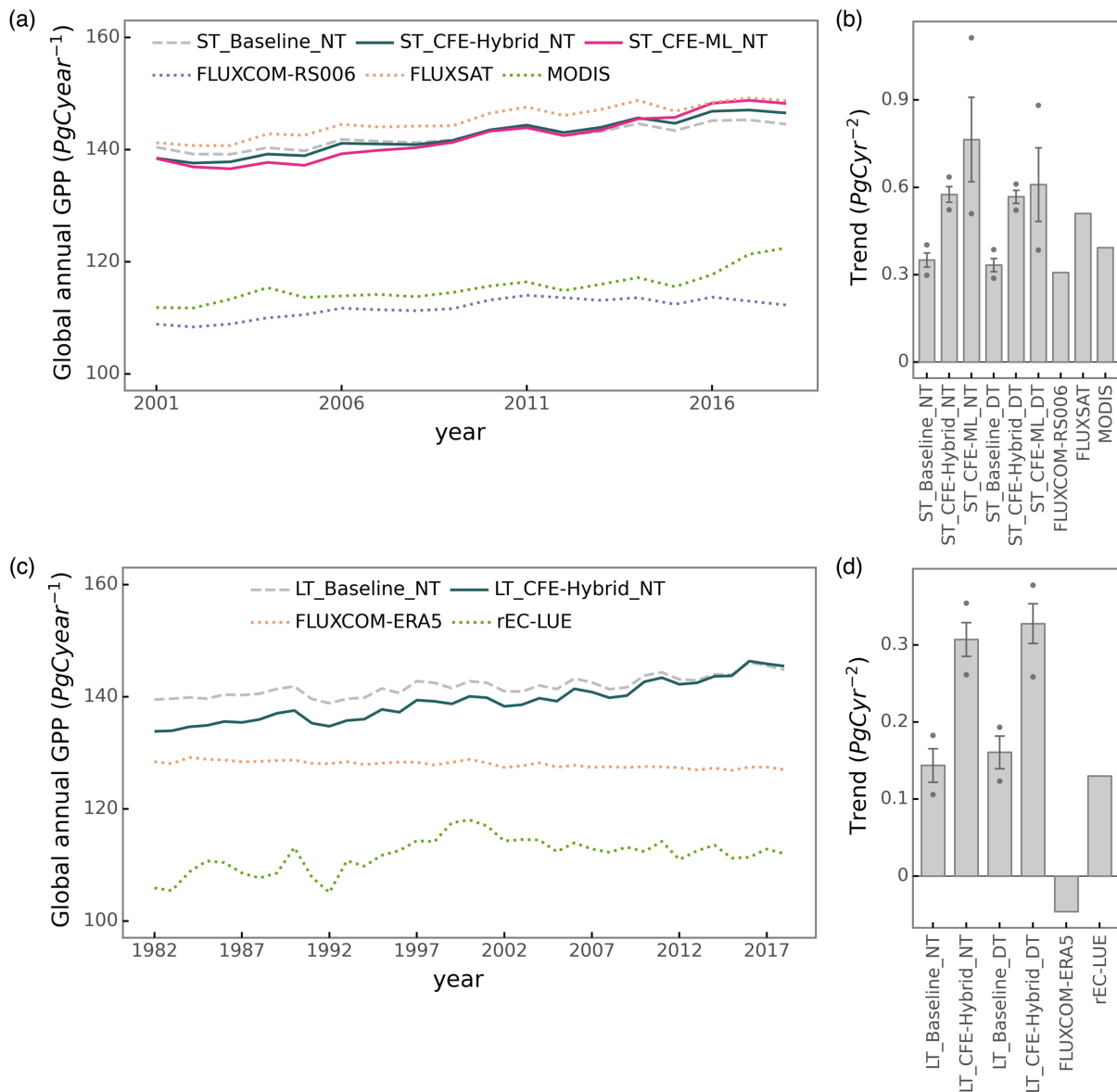
Figure 11. Global annual GPP variations (a) and trends (b) from 2001 to 2018 for
short-term CEDAR-GPP, FLUXCOM-RS006, FLUXSAT, and MODIS datasets.
Global annual GPP variations (c) and trends (d) over 1982 to 2018 for long-term for
long-term CEDAR-GPP, FLUXCOM-ERA5, and rEC-LUE datasets. Error bars in
(b) and (d) represent the 25% to 75% percentile from the model ensembles of
CEDAR-GPP. Dots in (b) and (d) indicate the minimum and maximum from the
model ensembles of CEDAR-GPP.

623 ## 3.3 GPP estimation uncertainties

624   We analyzed the spread between the 30 model ensemble members in CEDAR-GPP as an

625 indicator of uncertainties in GPP estimations. The spatial pattern of uncertainty in estimating annual

626 mean GPP largely resembled that of the mean map (Figure 12, Figure 6a). The largest model spread

627 was found in highly productive tropical forests, and this uncertainty decreased in temperate and cold

628 areas (Figure 12a). Tropical ecosystems, with a mean annual GPP between 1000 to 3500 $PgCyr^{-1}$,

629 only exhibited a 2% and 6% variation within the model ensemble (Figure 12b). Ecosystems in the

630 temperate and cold climates had a smaller annual GPP and proportionally small uncertainties of up

631 to 6%. However, ecosystems in Arid and Polar climates, despite their similarly low GPP, showed

632 higher model uncertainty, reaching 10% to 40% of the ensemble mean. The estimation uncertainty

633 of GPP trends was generally below 15% to 20% in the CEDAR-GPP datasets under the

634 ST_Baseline and ST_CFE-Hybrid setups (Figure 12c). However, in the ST_CFE-ML setup, the

635 estimation increased substantially, with model spread reaching up to 40% in tropical areas. Notably,

636 the long-term models showed a higher uncertainty compared to the short-term models.
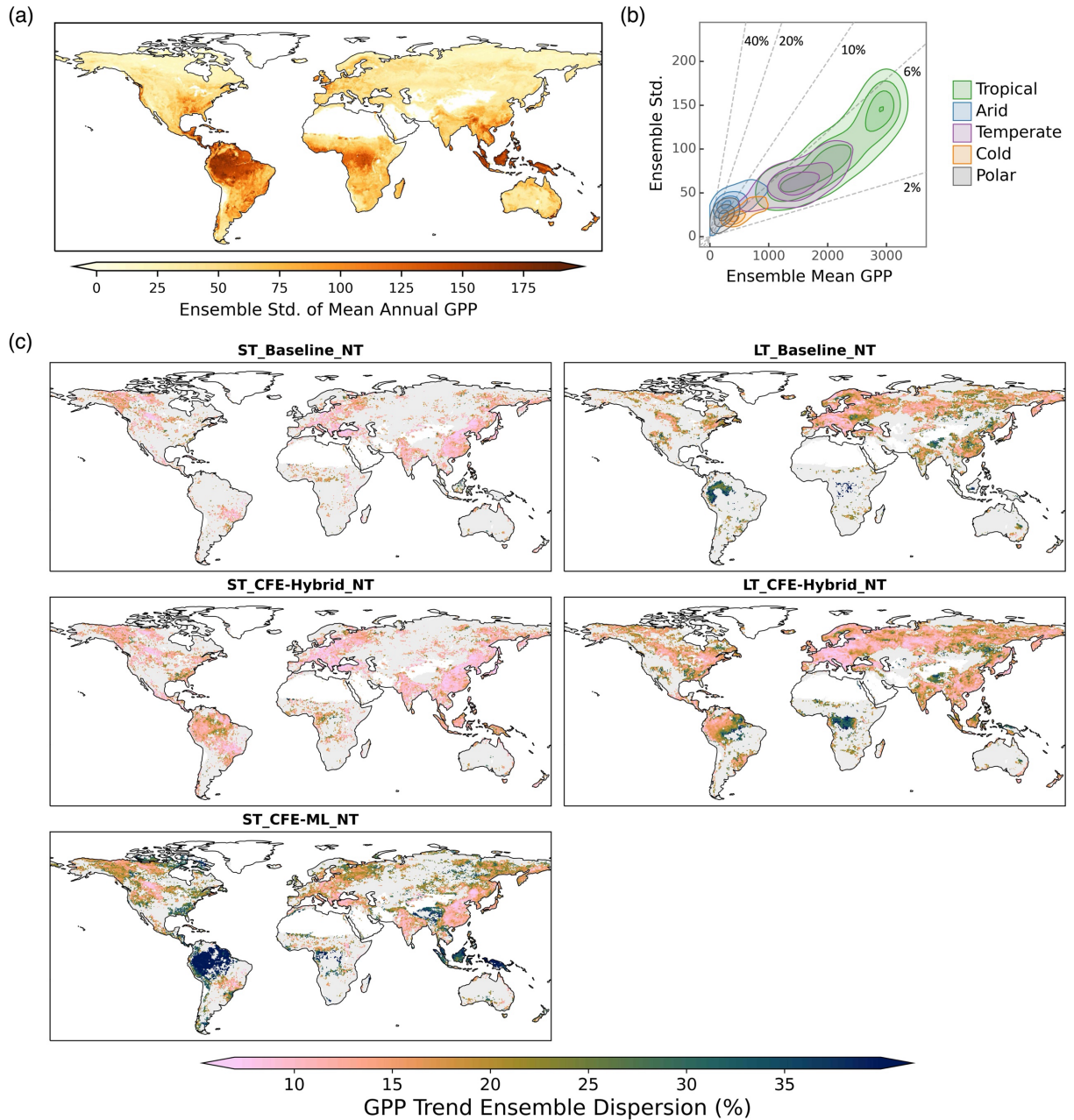
(a)

(b)

(c)

Figure 12. CEDAR-GPP estimation uncertainty derived from ensemble spread (standard deviation of 30 model predictions). (a) Spatial patterns of the absolute standard deviation from ensemble members in estimating the mean annual GPP from 2001 to 2018, using data from the ST_CFE-Hybrid_NT setup. (b) Relationships between ensemble standard deviation and ensemble mean in mean annual GPP. Colored contours denote clusters of Koppen climate zones. Dashed lines indicate the ratio between the ensemble standard deviation and the ensemble mean with values shown in percentage. (c) Spatial patterns of model uncertainty in GPP long-term trend estimation. Only areas where 90% of the ensemble members showed a statistically significant trend (p<0.05) are shown in the maps. The trend for the short-term datasets

32

648   (left column) was computed between 2001 to 2018. The trend for the long-term
649   datasets (right column) was computed between 1982 to 2018.

4. Discussion

4.1 Reducing uncertainties in GPP upscaling

Here we examine the three predominate sources of uncertainties in machine learning upscaling of GPP: eddy covariance measurements, input datasets, and the machine learning model. We discuss strategies used in CEDAR-GPP to reduce the impacts of these uncertainties and highlight potential future research directions.

4.1.1 Eddy covariance data

Uncertainties associated with eddy covariance measurement and data processing can propagate through the upscaling process. CEDAR-GPP was produced using monthly aggregated eddy covariance data, where the impact of random errors in half-hourly measurements was minimized due to the temporal aggregation (Jung et al., 2020). Our stringent quality screening further reduced data processing uncertainties such as those associated with gap-filling. Yet, the discrepancy in GPP patterns between the CEDAR-GPP NT and DT setups is indicative of systematic biases linked to the partitioning approaches used to derive GPP from the Net Ecosystem Exchange (NEE) measurements (Keenan et al., 2019; Pastorello et al., 2020). Interestingly, the mean annual GPP from the DT setup was slightly higher than that from the NT setup (Figure 6), and the DT setup also predicted a higher GPP trend in the long-term dataset (Figure 11). While these discrepancies were relatively small compared to the predominant spatiotemporal patterns, the separate DT and NT setups in CEDAR-GPP offered an interesting quantification of the GPP partitioning uncertainties over space and time, providing insights for future methodology improvements.

The unbalanced spatial representativeness of the eddy covariance data constitutes a more significant source of uncertainty, as highlighted by previous studies (Tramontana et al., 2015; Jung et al., 2020). Effective generalization of machine learning models requires a substantial volume of training data that adequately represents and balances unseen conditions. In CEDAR-GPP, this issue was mitigated with a large set of eddy covariance data (~18000 site-months) integrating FLUXNET2015 and two regional networks. However, data availability remains limited in critical

33

677 carbon exchange hotspots such as tropical, subtropical, and boreal regions, as well as in

678 mountainous areas (Figure 1). Contrary to widespread perception that sparse training data leads to

679 high upscaling uncertainties, our findings from the bootstrapped model spread indicated that modest

680 uncertainties in tropical areas relative to their high GPP magnitude (Figure 12). This observation

681 aligns with findings from the FLUXCOM product, revealing low extrapolation uncertainty in humid

682 tropical regions (Jung et al., 2020). Additionally, an early study found that a machine learning model,

683 when trained with simulated data from a terrestrial biosphere model that matches the locations and

684 times of FLUXNET sites, could explain 92% of the global variation of GPP (Jung et al., 2009).

685 These findings suggest that to fully understand the upscaling uncertainty, it is essential to evaluate

686 the generalization or extrapolation errors within the predictor space, which indicates the

687 environmental controls and physiological mechanisms of the ecosystem carbon fluxes (van der

688 Horst et al., 2019; Villarreal and Vargas, 2021). Nevertheless, data limitations in mountainous areas

689 and the absence of topology information in the predictor space in our models suggest potential

690 uncertainties related to topographical effects on GPP (Hao et al., 2022; Xie et al., 2023).

691 Furthermore, our analysis suggested that the estimated global GPP magnitudes were related

692 to the specific eddy covariance GPP data used in upscaling. Notably, global GPP magnitudes

693 derived from CEDAR-GPP closely aligned with those from FLUXSAT, while the estimates from

694 FLUXCOM were considerably lower (Figure 6, Figure 11). FLUXSAT used eddy covariance data

695 from FLUXNET2015, which largely overlapped with that included in CEDAR-GPP (Joiner and

696 Yoshida, 2020). FLUXCOM utilized data from FLUXNET La Thuile set and CarboAfrica network,

697 which consisted of a distinct set of sites (Tramontana et al., 2016). The influence from the predictor

698 datasets was minimal since all three datasets relied on MODIS-derived products. For a more in-

699 depth evaluation of the impacts of flux site representativeness on upscaling, future research

700 directions could include conducting synthetic experiments with simulations of ensembles of

701 terrestrial biosphere models.

702 4.1.2   Input predictors and controlling factors

703 Upscaled GPP inherent uncertainties from the input predictors, including satellite and climate

704 datasets. First, satellite remote sensing data contains noises resulting from sun-earth geometry,

705 atmospheric conditions, soil background, and geolocation inaccuracies. The models or algorithms

706 used for variable estimation, such as those for retrieving LAI, fAPAR, LST, and soil moisture, also

707 contain random errors and systematic biases specific to certain regions, biome types, or climatic

708 conditions (Yan et al., 2016b; Fang et al., 2019; Ma et al., 2019). Moreover, satellite observations

709 frequently contain missing values due to clouds, aerosols, snow, and algorithm failure, leading to

710 both systematic and random uncertainties. In producing CEDAR-GPP, we mitigated these

711 uncertainties through comprehensive preprocessing procedures. Our temporal gap-filling strategy

712 exploited both the temporal dependency of vegetation status and long-term climatology, to reduce

713 biases from missing values. Temporal and spatial aggregation further reduced the remaining data

714 gaps and random noises. Nevertheless, considerable uncertainties likely remained in satellite datasets

715 impacting the upscaled estimations.

716 A potentially more impactful source of uncertainty is the mismatch between the footprint of

717 the eddy covariance measurements and the coarse resolution of satellite observations. While flux

718 towers typically have a footprint of around ~1 km^2 (Chu et al., 2021), satellite observations

719 employed in CEDAR-GPP and most other upscaled datasets were at 5 km or lower resolution.

720 Systematic and random errors could be introduced due to this mismatch, particularly in

721 heterogenous biomes and areas with a mixture of vegetation and non-vegetated land covers. One

722 mitigation strategy is to generate upscaled datasets at a higher spatial resolution (e.g. 500m).

723 Alternatively, models could be trained at a high resolution and applied to the coarse resolution to

724 reduce computation and storage requirements (Dannenberg et al., 2023). However, this approach

725 does not address inherent scaling errors in coarse-resolution satellite images (Yan et al., 2016a; Dong

726 et al., 2023).

727 Besides the quality of predictors, successful machine learning upscaling also requires a

728 comprehensive set of features representing all controlling factors. For example, the lack of GPP

729 interannual variabilities in FLUXCOM-ERA5 manifests the importance of incorporating dynamic

730 vegetation signals from remote sensing in the upscaling framework. CEDAR-GPP used satellite

731 observations from optical, thermal, and microwave systems as well as climate variables thoroughly

732 representing GPP dynamics. Particularly, the inclusion of LST and soil moisture data provides

733 important information about resource limitations and stress factors, which are crucial for certain

734 biomes and/or under specific conditions (Stocker et al., 2018, 2019; Green et al., 2022). Dannenberg

735 et al. (2023) showed that incorporating LST from MODIS and soil moisture from the SMAP

736 satellite datasets substantially improved the machine learning estimation accuracy of GPP in North

737 American drylands. Nevertheless, accurately capturing interannual anomalies remains challenging for

738 certain biomes, such as evergreen needleleaf forest, cropland, and wetland (Figure 4), as

739 acknowledged by previous studies (Tramontana et al., 2016; Jung et al., 2020). This suggests that

740   vital information on GPP is missing or inadequately represented in existing datasets. To this end,

741   potential improvement may be achieved by incorporating datasets related to agricultural

742   management practices (crop type, cultivar, irrigation, fertilization) (Xie et al., 2021), plant hydraulic

743   and physiological properties (Liu et al., 2021), dynamic C4 plant distributions (Luo et al., 2024), root

744   and soil characteristics (Stocker et al., 2023), as well as topography (Xie et al., 2023).

745   4.1.3   Machine learning models and uncertainty quantification

746   The choice of machine learning models and their parameterization has been found to have a

747   relatively minor impact on GPP upscaling uncertainties (Tramontana et al., 2015). CEDAR used the

748   state-of-the-art boosting algorithm, XGBoost, which provided high performance given the current

749   data availability. Further reduction of model uncertainty will likely rely on additional information,

750   such as increasing the number of eddy covariance sites or incorporating more high-quality

751   predictors. Additionally, temporal dependency of carbon fluxes responses to atmospheric controls

752   may also be exploited with specialized deep neural networks such as recurrent neural networks or

753   transformers (Besnard et al., 2019; Ma and Liang, 2022).

754   A key challenge, however, is the quantification of uncertainties in machine learning upscaling

755   (Reichstein et al., 2019). The limited availability of eddy covariance data hinders a comprehensive

756   assessment of the extrapolation errors; consequently, metrics of predictive performance from cross-

757   validation are inherently biased. CEDAR derived estimation uncertainty for each GPP prediction

758   using bootstrapping model ensemble, which naturally mimics the biased sampling of flux tower

759   locations. Notably, the choice of input climate reanalysis datasets could also induce systematic

760   differences in GPP spatial and temporal patterns (Tramontana et al., 2015). As a result, the

761   FLUXCOM product generates model ensembles based on different reanalysis datasets to capture

762   these uncertainties. Additionally, different satellite datasets of vegetation structural proxies, such as

763   LAI, also exhibited significant discrepancies (Jiang et al., 2017). Thus, an ensemble approach

764   combining site-level bootstrapping with multiple sources of input predictors could potentially

765   provide a more comprehensive quantification of uncertainties. Future work may also explore

766   Bayesian neural networks, which provide uncertainty along with predictions and, at the same time,

767   present high predictive power comparable to ensemble tree-based algorithms (Ma et al., 2021).

4.2 Long-term GPP changes and CO$_2$ fertilization effect

CEDAR-GPP was constructed using a comprehensive set of climate variables and multi-source satellite observations, thus, encapsulating long-term GPP dynamics from both direct and indirect effects of climate controls. Particularly, CEDAR-GPP included the direct CO$_2$ fertilization effect, which has been shown to dominate the increasing trend of global photosynthesis (Chen et al., 2022). Incorporating these effects substantially improved long-term trends of GPP from site to global scales (Figure 5, 10, 11). CEDAR's CFE-Hybrid setup offered a conservative estimation of the direct CO$_2$ effects by simulating the light-limited sensitivity on LUE for C3 plants (Walker et al., 2021). Nevertheless, the model did not account for the impacts of nutrient availability, which could potentially constrain CO$_2$ fertilization (Reich et al., 2014; Peñuelas et al., 2017; Terrer et al., 2019). Furthermore, the sensitivity of light-limited photosynthesis is a function of temperature, resulting in the most pronounced increasing trend in the tropics (Figure 10). For simplicity, we assumed a fixed ratio of leaf internal to ambient CO$_2$ (χ) representing an average long-term value typical for C3 plants in the theoretical CO$_2$ sensitivity function. However, χ varies by environmental conditions, including temperature and vapor pressure deficit, and robustly modeling these dependencies remains challenging (Wang et al., 2017). Future work could incorporate more comprehensive representations of the χ and evaluate how the associated uncertainties affect the quantification of GPP and its temporal variations.

The CFE-ML model adopted a data-driven approach to infer CO$_2$ effects directly from eddy covariance data. This strategy allowed the model to capture any physiological pathways of the CO$_2$ impact evidenced in the eddy covariance measurements, including the increases of the biochemical rates as well as enhancements in the water use efficiency (Keenan et al., 2013). The model successfully detected a strong positive effect of CO$_2$ on eddy covariance measured GPP, consistent with previous studies based on process-based and statistical models (Fernández-Martínez et al., 2017; Ueyama et al., 2020; Chen et al., 2022). Notably, the CFE-ML model could have included the impacts of other factors that exhibit a strong temporal correlation with CO$_2$. For example, industrialization-induced increases in nitrogen deposition could synergistically boost GPP alongside CO$_2$ (O'Sullivan et al., 2019). Technological and management improvements in agriculture that contribute to a global boost of crop photosynthesis (Zeng et al., 2014), might also be indirectly reflected in the model estimates. As a result, the CFE-ML predicted a GPP trend that more closely aligned with eddy covariance observations, and the upscaled dataset also showed a globally higher

799   trend than CFE-Hybrid (Figure 5; Figure 10). Despite differences in magnitudes, spatial patterns of

800   GPP trends from the CFE-ML aligned with that from CFE-Hybrid, reflecting a strong temperature

801   dependency, implying that the effects of CO_2 likely remained the most significant factor.

802   Nonetheless, the considerable ensemble spread in the CO_2 trends from the CFE-ML model and

803   discrepancies between the CFE setups (Figure 11, Figure 13) underscored a high level of uncertainty

804   in the machine learning quantified CO_2 effects. Moreover, disentangling the direct CO_2 effects on

805   LUE, water use efficiency, and its indirect effects on fAPAR remains challenging with machine

806   learning models due to the correlations and interactions between CO_2 and other climatic or

807   environmental factors. Future work may exploit explainable machine learning and causal inference

808   to unravel the complex mechanisms and distinct pathways of CO_2 effects on vegetation carbon

809   uptake.

810   Our results suggested that variations in the estimated GPP long-term trends from different

811   products were largely related to the representation of CO_2 fertilization. Products that did not

812   consider the direct CO_2 effect, including our Baseline models, FLUXSAT, FLUXCOM, and

813   MODIS, showed minimal long-term changes in tropical GPP, while the CEDAR CFE-ML and

814   CFE-Hybrid models demonstrated significant GPP increases aligning with predictions from the

815   terrestrial biosphere models (Anav et al., 2015). FLUXCOM-ERA5, not accounting for dynamics

816   changes in vegetation structures and CO_2, did not capture either the direct or indirect CO_2

817   fertilization resulting in a slight negative GPP trend attributable to shifted climate patterns. Notably,

818   rEC-LUE exhibited contrasting trends before and after circa 2000, primarily attributed to changes in

819   vapor pressure deficit, PAR, and LAI, while the direct CO_2 fertilization effect remained consistent

820   (Zheng et al., 2020). Nevertheless, considerable differences between CEDAR-GPP and rEC-LUE,

821   as well as between our CFE-ML and CFE-Hybrid products, warrant more in-depth investigations

822   into long-term GPP responses to changes in atmospheric CO_2 and climate patterns.

823   5. Data availability and usage note

824   The CEDAR-GPP product, comprising ten GPP datasets, can be accessed at

825   https://zenodo.org/doi/10.5281/zenodo.8212706 (Kang et al., 2024). These datasets were

826   generated at a spatial resolution of 0.05° and monthly time steps. Each dataset includes an ensemble

827   mean GPP ("GPP_mean") and an ensemble standard deviation ("GPP_std"). Data is formatted in

828   netCDF with the following naming convention: "CEDAR-GPP_<version>_<model

829   setup>_<YYYYMM>.nc".

830   The CEDAR GPP product offers GPP estimates derived from ten different models. Models

831   are characterized by 1) temporal coverage, 2) configuration of CO2 fertilization, and 3) GPP

832   partitioning approach (Table 2). We provide a structured approach to selecting the most appropriate

833   dataset for research or applications.

834   1) Study period considerations: the Short-Term (ST) setup is ideal for studies focusing on

835   periods after 2000. These models are constructed using a broader range of explanatory predictors,

836   offering higher precision and smaller random errors. The Long-Term (LT) datasets shall be used for

837   research assessing GPP dynamics over a longer time period (before 2001). It is important to note

838   that trends from the ST and LT datasets are not directly comparable, as they were derived from

839   different satellite remote sensing data.

840   2) CO_2 Fertilization Effect (CFE) configurations: the CFE-Hybrid and CFE-ML setups are

841   preferable when assessing temporal GPP dynamics, especially long-term trends. The CFE-Hybrid

842   setup includes a hypothetical trend for the direct CO_2 effect, while CFE-ML is purely data-driven

843   and does not make any specific assumption about the sensitivity of photosynthesis to CO_2.

844   Averaging the CFE-Hybrid and CFE-ML estimates is acceptable, with the difference between them

845   reflecting the uncertainty surrounding the direct CO_2 effect. Note that the Baseline setup shall not

846   be used to study long-term GPP dynamics, especially those induced by elevated CO_2. Baseline setup

847   may be useful to compare with other remote sensing-derived GPP datasets that do not consider the

848   direct CO_2 effect. Differences between these setups regarding mean GPP spatial patterns, seasonal

849   and interannual variations are considered to be minor.

850   3) GPP partitioning methods: We recommend using the mean value derived from both the

851   "NT" (Nighttime) and "DT" (Daytime). The difference between these two provides insight into the

852   uncertainties arising from the partitioning approaches used in GPP estimation from eddy covariance

853   measurements.

6. Code availability

855   The code for upscaling and generating global GPP datasets can be accessed at

856   https://doi.org/10.5281/zenodo.8400968.

7. Conclusions

We present the CEDAR-GPP product generated by upscaling global eddy covariance measurements with machine learning and a broad range of satellite and climate variables. CEDAR-GPP comprises four long-term datasets from 1982 to 2020 and six short-term datasets from 2001 to 2020. These datasets encompass three configurations regarding the incorporation of direct CO_2 fertilization effects and two partitioning approaches to derive GPP from eddy covariance data. The machine learning models of CEDAR-GPP demonstrated high capability in predicting monthly GPP, its seasonal cycles, and spatial variability within the global eddy covariance sites, with cross-validated R^2 between 0.56 to 0.79. Short-term model setups consistently outperformed long-term models due to considerably more and higher-quality information from multi-source satellite observations.

CEDAR-GPP advances satellite-based GPP estimations, as the first upscaled dataset that considered the direct biochemical effects of elevated atmospheric CO_2 on photosynthesis, which is responsible for an increasing land carbon sink over the past decades. We showed that incorporating this effect in our CFE-ML and CFE-Hybrid models substantially improved the estimation of GPP trends at eddy covariance sites. Global patterns of long-term GPP trends in the CFE-ML setups showed a strong temperature dependency consistent with biophysical theories. Aside from the trend, global spatial and temporal GPP patterns from CEDAR generally aligned with other satellite-based GPP datasets.

In conclusion, CEDAR-GPP, informed by global eddy covariance measurements and a broad range of multi-source remote sensing observations and climatic variables, offered a comprehensive representation of global GPP spatial and temporal dynamics over the past four decades. The different CO_2 fertilization configures integrated in CEDAR-GPP offer new opportunities for understanding global ecosystem photosynthesis's response to increases in atmospheric CO_2 along different pathways over space and time. CEDAR-GPP is expected to serve as a valuable tool for benchmarking process-based modeling and constraining the global carbon cycle.

Appendix A: Photosynthesis sensitivity function of CO_2

The Light Use Efficiency (LUE) model (Monteith, 1972) of GPP states that,

$$GPP = APAR \times LUE = PAR \times fAPAR \times LUE \tag{A1}$$

where PAR is the photosynthetic active radiation, $fAPAR$ is the fraction of PAR that plant canopy has absorbed, and $APAR$ is the absorbed PAR. Eco-evolutionary theory predicts that the electron-transport-limited (light-limited) (A_j) and Rubisco-limited (A_c) rates of photosynthesis converge on the time scale of physiological acclimation, which is in the order of a few weeks (Harrison et al., 2021; Wang et al., 2017). Thus, at a monthly time scale, we assume that

$$A = A_c = A_j \tag{A2}$$

where A is the gross photosynthetic rate, here equivalent to GPP.

In the following, we derive our sensitivity function based on A_j, which has a smaller response to CO_2 than A_c, thus providing conservative estimates of the direct CO_2 fertilization effect (Walker et al., 2021). According to the Fauquhar, von Caemmerer and Berry (FvCB) model (Farquhar et al., 1980),

$$A_j = \varphi_0 I \frac{c_i - \Gamma^*}{c_i + 2\Gamma^*} \tag{A3}$$

where φ_0 is the intrinsic quantum efficiency of photosynthesis, I is the absorbed PAR ($I = APAR$), c_i is the leaf-internal partial pressure of CO_2, and Γ^* is the photorespiratory compensation point that depends on temperature:

$$\Gamma^* = r_{25} e^{\frac{\Delta H(T - 298.15)}{298.15RT}} \tag{A4}$$

where $r_{25} = 4.22\ Pa$ is the photorespiratory point at 25 °C, ΔH is the activation energy ($37.83 \cdot 10^3$ J mol^{-1}), T is the air temperature in Kelvin, and R is the molar gas constant (8.314 J mol^{-1} K^{-1}. We denote atmospheric CO_2 concentration as c_a, and χ is the ratio of leaf internal and external CO_2, so

$$c_i = \chi c_a \tag{A5}$$

Combing (A1), (A3), (A5), and assuming (A2), LUE can be written as,

$$LUE = \varphi_0 \frac{c_i - \Gamma^*}{c_i + 2\Gamma^*} = \varphi_0 \frac{\chi c_a - \Gamma^*}{\chi c_a + 2\Gamma^*} \tag{A6}$$

We can therefore show that under constant absorbed light (I or $APAR$), the sensitivity of GPP to CO_2 is proportional to that of LUE,

$$\frac{\partial GPP}{\partial c_a} = \frac{\partial \varphi_0 I \frac{\chi c_a - \Gamma^*}{\chi c_a + 2\Gamma^*}}{\partial c_a} = I \frac{\partial LUE}{\partial c_a} \tag{A7}$$

911   Thus from (A7), we can express the actual GPP at the time t and a CO_2 level c_a^t as the product of a

912   reference GPP with a CO_2 level c_a^0 and the ratio between actual and reference LUE (A8-9). We

913   denote the actual GPP as time t as $GPP^t_{c_a=c_a^t}$, and the reference GPP at time t as $GPP^t_{c_a=c_a^0}$.

914
$$\frac{GPP^t_{c_a=c_a^t}}{GPP^t_{c_a=c_a^0}} = \frac{LUE^t_{c_a=c_a^t}}{LUE^t_{c_a=c_a^0}} = \frac{\frac{\chi c_a^t - \Gamma^*}{\chi c_a^t + 2\Gamma^*}}{\frac{\chi c_a^0 - \Gamma^*}{\chi c_a^0 + 2\Gamma^*}} = \frac{\phi^t_{CO2}}{\phi^{t_0}_{CO2}} \tag{A8}$$

915
$$GPP^t_{c_a=c_a^t} = GPP^t_{c_a=c_a^0} \times \frac{\phi^t_{CO2}}{\phi^{t_0}_{CO2}} \tag{A9}$$

916   The reference GPP represents the GPP value at time t if the CO_2 were at the level of a reference

917   level, while all other factors, such as PAR, $fAPAR$, temperature, and other environmental controls

918   remain unchanged. Here the CO_2 impacts on LUE depend on atmospheric CO_2 (c_a), χ , and air

919   temperature. We fixed χ to the global long-term average value 0.7 typical to C3 plants (Prentice et

920   al., 2014; Wang et al., 2017).

921   In the CFE-Hybrid model, we estimated the reference GPP by fixing the CO_2 at the level of the

922   year 2001 while keeping all other variables dynamic in the CFE-ML model. Then the actual GPP can

923   be estimated following (A9). Fixing CO_2 values to the 2001 level, the start year of eddy covariance

924   data used in model training, essentially removed the effects of CO_2 inferred by the CFE-ML model.

925   **Supplement**

926   The supplement related to this article is available online.

927   **Author contributions**

928   T. K. and Y. K. conceptualized the study. Y. K. performed the formal analysis and generated

929   the final product. Y. K., T. K., M. B., and M. G. contributed to the development and investigation

930   of the research. Y. K., M. G., and X. L. contributed to data curation and processing. Y. K. prepared

931   the manuscript with contributions from all co-authors. T. K. supervised the project.

943 **References**

944 Anav, A., Friedlingstein, P., Beer, C., Ciais, P., Harper, A., Jones, C., Murray-Tortarolo, G., Papale,
945 D., Parazoo, N. C., Peylin, P., Piao, S., Sitch, S., Viovy, N., Wiltshire, A., and Zhao, M.:
946 Spatiotemporal patterns of terrestrial gross primary production: A review, Reviews of Geophysics,
947 1–34, https://doi.org/10.1002/2015RG000483, 2015.

948 Badgley, G., Anderegg, L. D. L., Berry, J. A., and Field, C. B.: Terrestrial gross primary production:
949 Using NIRV to scale from site to globe, Global Change Biology, 25, 3731–3740,
950 https://doi.org/10.1111/gcb.14729, 2019.

951 Baldocchi, D. D.: How eddy covariance flux measurements have contributed to our understanding
952 of Global Change Biology, Global Change Biology, 26, 242–260,
953 https://doi.org/10.1111/gcb.14807, 2020.

954 Beck, H. E., Zimmermann, N. E., McVicar, T. R., Vergopolan, N., Berg, A., and Wood, E. F.:
955 Present and future köppen-geiger climate classification maps at 1-km resolution, Scientific Data, 5,
956 1–12, https://doi.org/10.1038/sdata.2018.214, 2018.

957 Beer, C., Reichstein, M., Tomelleri, E., Ciais, P., Jung, M., Carvalhais, N., Rödenbeck, C., Arain, M.
958 A., Baldocchi, D., Bonan, G. B., Bondeau, A., Cescatti, A., Lasslop, G., Lindroth, A., Lomas, M.,
959 Luyssaert, S., Margolis, H., Oleson, K. W., Roupsard, O., Veenendaal, E., Viovy, N., Williams, C.,
960 Woodward, F. I., and Papale, D.: Terrestrial gross carbon dioxide uptake: Global distribution and
961 covariation with climate, Science, 329, 834–838, https://doi.org/10.1126/science.1184984, 2010.

962 Berdugo, M., Gaitán, J. J., Delgado-Baquerizo, M., Crowther, T. W., and Dakos, V.: Prevalence and
963 drivers of abrupt vegetation shifts in global drylands, Proceedings of the National Academy of
964 Sciences, 119, e2123393119, https://doi.org/10.1073/pnas.2123393119, 2022.

965 Besnard, S., Carvalhais, N., Altaf Arain, M., Black, A., Brede, B., Buchmann, N., Chen, J., Clevers, J.
966 G. P. W., Dutrieux, L. P., Gans, F., Herold, M., Jung, M., Kosugi, Y., Knohl, A., Law, B. E., Paul-
967 Limoges, E., Lohila, A., Merbold, L., Roupsard, O., Valentini, R., Wolf, S., Zhang, X., and
968 Reichstein, M.: Memory effects of climate and vegetation affecting net ecosystem CO2 fluxes in
969 global forests, PLoS ONE, 14, 1–22, https://doi.org/10.1371/journal.pone.0211510, 2019.

970   Bloomfield, K. J., Stocker, B. D., Keenan, T. F., and Prentice, I. C.: Environmental controls on the
971   light use efficiency of terrestrial gross primary production, Global Change Biology, 29, 1037–1053,
972   https://doi.org/10.1111/gcb.16511, 2023.

973   Campbell, J. E., Berry, J. A., Seibt, U., Smith, S. J., Montzka, S. A., Launois, T., Belviso, S., Bopp, L.,
974   and Laine, M.: Large historical growth in global terrestrial gross primary production, Nature, 544,
975   84–87, https://doi.org/10.1038/nature22030, 2017.

976   Camps-Valls, G., Campos-Taberner, M., Moreno-Martínez, Á., Walther, S., Duveiller, G., Cescatti,
977   A., Mahecha, M. D., Muñoz-Marí, J., García-Haro, F. J., Guanter, L., Jung, M., Gamon, J. A.,
978   Reichstein, M., and Running, S. W.: A unified vegetation index for quantifying the terrestrial
979   biosphere, Science Advances, 7, eabc7447, https://doi.org/10.1126/sciadv.abc7447, 2021.

980   Cao, S., Li, M., Zhu, Z., Zha, J., Zhao, W., Duanmu, Z., Chen, J., Zheng, Y., and Chen, Y.:
981   Spatiotemporally consistent global dataset of the GIMMS Leaf Area Index (GIMMS LAI4g) from
982   1982 to 2020, Earth System Science Data Discussions, 1–31, https://doi.org/10.5194/essd-2023-68,
983   2023.

984   Chen, C., Park, T., Wang, X., Piao, S., Xu, B., Chaturvedi, R. K., Fuchs, R., Brovkin, V., Ciais, P.,
985   Fensholt, R., Tømmervik, H., Bala, G., Zhu, Z., Nemani, R. R., and Myneni, R. B.: China and India
986   lead in greening of the world through land-use management, Nature Sustainability, 2, 122–129,
987   https://doi.org/10.1038/s41893-019-0220-7, 2019.

988   Chen, C., Riley, W. J., Prentice, I. C., and Keenan, T. F.: CO2 fertilization of terrestrial
989   photosynthesis inferred from site to global scales, Proceedings of the National Academy of Sciences,
990   119, 1–8, https://doi.org/10.1073/pnas.2115627119/, 2022.

991   Chen, T. and Guestrin, C.: XGBoost: a scalable tree boosting system, in: Proceedings of the 22nd
992   ACM SIGKDD International Conference on Knowledge Discovery and Data Mining - KDD '16,
993   785–794, https://doi.org/10.1145/2939672.2939785, 2016.

994   Chu, H., Luo, X., Ouyang, Z., Chan, W. S., Dengel, S., Biraud, S. C., Torn, M. S., Metzger, S.,
995   Kumar, J., Arain, M. A., Arkebauer, T. J., Baldocchi, D., Bernacchi, C., Billesbach, D., Black, T. A.,
996   Blanken, P. D., Bohrer, G., Bracho, R., Brown, S., Brunsell, N. A., Chen, J., Chen, X., Clark, K.,
997   Desai, A. R., Duman, T., Durden, D., Fares, S., Forbrich, I., Gamon, J. A., Gough, C. M., Griffis, T.,
998   Helbig, M., Hollinger, D., Humphreys, E., Ikawa, H., Iwata, H., Ju, Y., Knowles, J. F., Knox, S. H.,
999   Kobayashi, H., Kolb, T., Law, B., Lee, X., Litvak, M., Liu, H., Munger, J. W., Noormets, A., Novick,
1000 K., Oberbauer, S. F., Oechel, W., Oikawa, P., Papuga, S. A., Pendall, E., Prajapati, P., Prueger, J.,
1001 Quinton, W. L., Richardson, A. D., Russell, E. S., Scott, R. L., Starr, G., Staebler, R., Stoy, P. C.,
1002 Stuart-Haëntjens, E., Sonnentag, O., Sullivan, R. C., Suyker, A., Ueyama, M., Vargas, R., Wood, J.
1003 D., and Zona, D.: Representativeness of Eddy-Covariance flux footprints for areas surrounding
1004 AmeriFlux sites, Agricultural and Forest Meteorology, 301–302,
1005 https://doi.org/10.1016/j.agrformet.2021.108350, 2021.

1006 Dannenberg, M. P., Barnes, M. L., Smith, W. K., Johnston, M. R., Meerdink, S. K., Wang, X., Scott,
1007 R. L., and Biederman, J. A.: Upscaling dryland carbon and water fluxes with artificial neural
1008 networks of optical, thermal, and microwave satellite remote sensing, Biogeosciences, 20, 383–404,
1009 https://doi.org/10.5194/bg-20-383-2023, 2023.

1010   De Kauwe, M. G., Keenan, T. F., Medlyn, B. E., Prentice, I. C., and Terrer, C.: Satellite based
1011   estimates underestimate the effect of CO2 fertilization on net primary productivity, Nature Climate
1012   Change, 6, 892–893, https://doi.org/10.1038/nclimate3105, 2016.

1013   Dong, Y., Li, J., Jiao, Z., Liu, Q., Zhao, J., Xu, B., Zhang, H., Zhang, Z., Liu, C., Knyazikhin, Y., and
1014   Myneni, R. B.: A Method for Retrieving Coarse-Resolution Leaf Area Index for Mixed Biomes
1015   Using a Mixed-Pixel Correction Factor, IEEE Transactions on Geoscience and Remote Sensing, 61,
1016   1–17, https://doi.org/10.1109/TGRS.2023.3235949, 2023.

1017   Dorigo, W., Wagner, W., Albergel, C., Albrecht, F., Balsamo, G., Brocca, L., Chung, D., Ertl, M.,
1018   Forkel, M., Gruber, A., Haas, E., Hamer, P. D., Hirschi, M., Ikonen, J., de Jeu, R., Kidd, R., Lahoz,
1019   W., Liu, Y. Y., Miralles, D., Mistelbauer, T., Nicolai-Shaw, N., Parinussa, R., Pratola, C., Reimer, C.,
1020   van der Schalie, R., Seneviratne, S. I., Smolander, T., and Lecomte, P.: ESA CCI Soil Moisture for
1021   improved Earth system understanding: State-of-the art and future directions, Remote Sensing of
1022   Environment, 203, 185–215, https://doi.org/10.1016/j.rse.2017.07.001, 2017.

1023   Dorigo, W. A., Gruber, A., De Jeu, R. A. M., Wagner, W., Stacke, T., Loew, A., Albergel, C., Brocca,
1024   L., Chung, D., Parinussa, R. M., and Kidd, R.: Evaluation of the ESA CCI soil moisture product
1025   using ground-based observations, Remote Sensing of Environment, 162,
1026   https://doi.org/10.1016/j.rse.2014.07.023, 2015.

1027   Ehlers, I., Augusti, A., Betson, T. R., Nilsson, M. B., Marshall, J. D., and Schleucher, J.: Detecting
1028   long-term metabolic shifts using isotopomers: CO2-driven suppression of photorespiration in C3
1029   plants over the 20th century, Proceedings of the National Academy of Sciences, 112, 15585–15590,
1030   https://doi.org/10.1073/pnas.1504493112, 2015.

1031   Fang, H., Baret, F., Plummer, S., and Schaepman-Strub, G.: An overview of global leaf area index
1032   (LAI): Methods, products, validation, and applications, Reviews of Geophysics, 2018RG000608,
1033   https://doi.org/10.1029/2018RG000608, 2019.

1034   Farquhar, G. D., von Caemmerer, S., and Berry, J. A.: A biochemical model of photosynthetic CO2
1035   assimilation in leaves of C3 species, Planta, 149, 78–90, https://doi.org/10.1007/BF00386231,
1036   1980.

1037   Fernández-Martínez, M., Vicca, S., Janssens, I. A., Ciais, P., Obersteiner, M., Bartrons, M., Sardans,
1038   J., Verger, A., Canadell, J. G., Chevallier, F., Wang, X., Bernhofer, C., Curtis, P. S., Gianelle, D.,
1039   Grünwald, T., Heinesch, B., Ibrom, A., Knohl, A., Laurila, T., Law, B. E., Limousin, J. M., Longdoz,
1040   B., Loustau, D., Mammarella, I., Matteucci, G., Monson, R. K., Montagnani, L., Moors, E. J.,
1041   Munger, J. W., Papale, D., Piao, S. L., and Peñuelas, J.: Atmospheric deposition, CO2, and change in
1042   the land carbon sink, Sci Rep, 7, 9632, https://doi.org/10.1038/s41598-017-08755-8, 2017.

1043   Friedl, M. and Sulla-Menashe, D.: MCD12Q1 MODIS/Terra+Aqua Land Cover Type Yearly L3
1044   Global 500m SIN Grid V006 [Data set], NASA EOSDIS Land Processes DAAC,
1045   https://doi.org/10.5067/MODIS/MCD12Q1.006, 2019.

1046   Friedlingstein, P., Meinshausen, M., Arora, V. K., Jones, C. D., Anav, A., Liddicoat, S. K., and
1047   Knutti, R.: Uncertainties in CMIP5 climate projections due to carbon cycle feedbacks, Journal of
1048   Climate, 27, 511–526, https://doi.org/10.1175/JCLI-D-12-00579.1, 2014.

1049   Friedlingstein, P., O'Sullivan, M., Jones, M. W., Andrew, R. M., Gregor, L., Hauck, J., Le Quéré, C.,
1050   Luijkx, I. T., Olsen, A., Peters, G. P., Peters, W., Pongratz, J., Schwingshackl, C., Sitch, S., Canadell,
1051   J. G., Ciais, P., Jackson, R. B., Alin, S. R., Alkama, R., Arneth, A., Arora, V. K., Bates, N. R., Becker,
1052   M., Bellouin, N., Bittig, H. C., Bopp, L., Chevallier, F., Chini, L. P., Cronin, M., Evans, W., Falk, S.,
1053   Feely, R. A., Gasser, T., Gehlen, M., Gkritzalis, T., Gloege, L., Grassi, G., Gruber, N., Gürses, Ö.,
1054   Harris, I., Hefner, M., Houghton, R. A., Hurtt, G. C., Iida, Y., Ilyina, T., Jain, A. K., Jersild, A.,
1055   Kadono, K., Kato, E., Kennedy, D., Klein Goldewijk, K., Knauer, J., Korsbakken, J. I.,
1056   Landschützer, P., Lefèvre, N., Lindsay, K., Liu, J., Liu, Z., Marland, G., Mayot, N., McGrath, M. J.,
1057   Metzl, N., Monacci, N. M., Munro, D. R., Nakaoka, S.-I., Niwa, Y., O'Brien, K., Ono, T., Palmer, P.
1058   I., Pan, N., Pierrot, D., Pocock, K., Poulter, B., Resplandy, L., Robertson, E., Rödenbeck, C.,
1059   Rodriguez, C., Rosan, T. M., Schwinger, J., Séférian, R., Shutler, J. D., Skjelvan, I., Steinhoff, T., Sun,
1060   Q., Sutton, A. J., Sweeney, C., Takao, S., Tanhua, T., Tans, P. P., Tian, X., Tian, H., Tilbrook, B.,
1061   Tsujino, H., Tubiello, F., van der Werf, G. R., Walker, A. P., Wanninkhof, R., Whitehead, C.,
1062   Willstrand Wranne, A., et al.: Global Carbon Budget 2022, Earth System Science Data, 14, 4811–
1063   4900, 2023.

1064   Gampe, D., Zscheischler, J., Reichstein, M., Sullivan, M. O., Smith, W. K., Sitch, S., and Buermann,
1065   W.: Increasing impact of warm droughts on northern ecosystem productivity over recent decades,
1066   Nature Climate Change, https://doi.org/10.1038/s41558-021-01112-8, 2021.

1067   Gao, B. C.: NDWI - A normalized difference water index for remote sensing of vegetation liquid
1068   water from space, Remote Sensing of Environment, 58, 257–266, https://doi.org/10.1016/S0034-
1069   4257(96)00067-3, 1996.

1070   Gitelson, A. A.: Remote estimation of leaf area index and green leaf biomass in maize canopies,
1071   Geophysical Research Letters, 30, 1248, https://doi.org/10.1029/2002GL016450, 2003.

1072   Green, J. K., Ballantyne, A., Abramoff, R., Gentine, P., Makowski, D., and Ciais, P.: Surface
1073   temperatures reveal the patterns of vegetation water stress and their environmental drivers across
1074   the tropical Americas, Global Change Biology, 28, 2940–2955, https://doi.org/10.1111/gcb.16139,
1075   2022.

1076   Gruber, A., Scanlon, T., Van Der Schalie, R., Wagner, W., and Dorigo, W.: Evolution of the ESA
1077   CCI Soil Moisture climate data records and their underlying merging methodology, Earth System
1078   Science Data, 11, 717–739, https://doi.org/10.5194/essd-11-717-2019, 2019.

1079   Hao, D., Bisht, G., Huang, M., Ma, P.-L., Tesfa, T., Lee, W.-L., Gu, Y., and Leung, L. R.: Impacts of
1080   Sub-Grid Topographic Representations on Surface Energy Balance and Boundary Conditions in the
1081   E3SM Land Model: A Case Study in Sierra Nevada, Journal of Advances in Modeling Earth
1082   Systems, 14, e2021MS002862, https://doi.org/10.1029/2021MS002862, 2022.

1083   Harrison, S. P., Cramer, W., Franklin, O., Prentice, I. C., Wang, H., Brännström, Å., de Boer, H.,
1084   Dieckmann, U., Joshi, J., Keenan, T. F., Lavergne, A., Manzoni, S., Mengoli, G., Morfopoulos, C.,
1085   Peñuelas, J., Pietsch, S., Rebel, K. T., Ryu, Y., Smith, N. G., Stocker, B. D., and Wright, I. J.: Eco-
1086   evolutionary optimality as a means to improve vegetation and land-surface models, New Phytologist,
1087   https://doi.org/10.1111/nph.17558, 2021.

1088   Haverd, V., Smith, B., Canadell, J. G., Cuntz, M., Mikaloff-Fletcher, S., Farquhar, G., Woodgate, W.,
1089   Briggs, P. R., and Trudinger, C. M.: Higher than expected CO2 fertilization inferred from leaf to
1090   global observations, Global Change Biology, 26, 2390–2402, https://doi.org/10.1111/gcb.14950,
1091   2020.

1092   van der Horst, S. V. J., Pitman, A. J., De Kauwe, M. G., Ukkola, A., Abramowitz, G., and Isaac, P.:
1093   How representative are FLUXNET measurements of surface fluxes during temperature extremes?,
1094   Biogeosciences, 16, 1829–1844, https://doi.org/10.5194/bg-16-1829-2019, 2019.

1095   Jiang, C., Ryu, Y., Fang, H., Myneni, R., Claverie, M., and Zhu, Z.: Inconsistencies of interannual
1096   variability and trends in long-term satellite leaf area index products, Global Change Biology, 23,
1097   4133–4146, https://doi.org/10.1111/gcb.13787, 2017.

1098   Joiner, J. and Yoshida, Y.: Satellite-based reflectances capture large fraction of variability in global
1099   gross primary production (GPP) at weekly time scales, Agricultural and Forest Meteorology, 291,
1100   108092, https://doi.org/10.1016/j.agrformet.2020.108092, 2020.

1101   Jung, M., Reichstein, M., and Bondeau, A.: Towards global empirical upscaling of FLUXNET eddy
1102   covariance observations: Validation of a model tree ensemble approach using a biosphere model,
1103   Biogeosciences, 6, 2001–2013, https://doi.org/10.5194/bg-6-2001-2009, 2009.

1104   Jung, M., Reichstein, M., Margolis, H. A., Cescatti, A., Richardson, A. D., Arain, M. A., Arneth, A.,
1105   Bernhofer, C., Bonal, D., Chen, J., Gianelle, D., Gobron, N., Kiely, G., Kutsch, W., Lasslop, G.,
1106   Law, B. E., Lindroth, A., Merbold, L., Montagnani, L., Moors, E. J., Papale, D., Sottocornola, M.,
1107   Vaccari, F., and Williams, C.: Global patterns of land-atmosphere fluxes of carbon dioxide , latent
1108   heat , and sensible heat derived from eddy covariance , satellite , and meteorological observations,
1109   Journal of Geophysical Research: Biogeosciences, 116, 1–16,
1110   https://doi.org/10.1029/2010JG001566, 2011.

1111   Jung, M., Reichstein, M., Schwalm, C. R., Huntingford, C., Sitch, S., Ahlström, A., Arneth, A.,
1112   Camps-Valls, G., Ciais, P., Friedlingstein, P., Gans, F., Ichii, K., Jain, A. K., Kato, E., Papale, D.,
1113   Poulter, B., Raduly, B., Rödenbeck, C., Tramontana, G., Viovy, N., Wang, Y. P., Weber, U., Zaehle,
1114   S., and Zeng, N.: Compensatory water effects link yearly global land CO 2 sink changes to
1115   temperature, Nature, 541, 516–520, https://doi.org/10.1038/nature20780, 2017.

1116   Jung, M., Schwalm, C., Migliavacca, M., Walther, S., Camps-Valls, G., Koirala, S., Anthoni, P.,
1117   Besnard, S., Bodesheim, P., Carvalhais, N., Chevallier, F., Gans, F., S Goll, D., Haverd, V., Köhler,
1118   P., Ichii, K., K Jain, A., Liu, J., Lombardozzi, D., E M S Nabel, J., A Nelson, J., O'Sullivan, M.,
1119   Pallandt, M., Papale, D., Peters, W., Pongratz, J., Rödenbeck, C., Sitch, S., Tramontana, G., Walker,
1120   A., Weber, U., and Reichstein, M.: Scaling carbon fluxes from eddy covariance sites to globe:
1121   Synthesis and evaluation of the FLUXCOM approach, Biogeosciences, 17, 1343–1365,
1122   https://doi.org/10.5194/bg-17-1343-2020, 2020.

1123   Kang, Y., Ozdogan, M., Zhu, X., Ye, Z., Hain, C., and Anderson, M.: Comparative assessment of
1124   environmental variables and machine learning algorithms for maize yield prediction in the US
1125   Midwest, Environmental Research Letters, 15, https://doi.org/10.1088/1748-9326/ab7df9, 2020.

1126   Kang, Y., Gaber, M., Bassiouni, M., Lu, X., and Keenan, T.: CEDAR-GPP: A Spatiotemporally
1127   Upscaled Dataset of Gross Primary Productivity Incorporating CO2 Fertilization (v1.0),
1128   https://doi.org/10.5281/zenodo.8212706, 2024.

1129   Keeling, R. F., Graven, H. D., Welp, L. R., Resplandy, L., Bi, J., Piper, S. C., Sun, Y., Bollenbacher,
1130   A., and Meijer, H. A. J.: Atmospheric evidence for a global secular increase in carbon isotopic
1131   discrimination of land photosynthesis, Proceedings of the National Academy of Sciences of the
1132   United States of America, 114, 10361–10366, https://doi.org/10.1073/pnas.1619240114, 2017.

1133   Keenan, T. F., Hollinger, D. Y., Bohrer, G., Dragoni, D., Munger, J. W., Schmid, H. P., and
1134   Richardson, A. D.: Increase in forest water-use efficiency as atmospheric carbon dioxide
1135   concentrations rise, Nature, 499, 324–327, https://doi.org/10.1038/nature12291, 2013.

1136   Keenan, T. F., Prentice, I. C., Canadell, J. G., Williams, C. A., Wang, H., Raupach, M., and Collatz,
1137   G. J.: Recent pause in the growth rate of atmospheric CO2 due to enhanced terrestrial carbon
1138   uptake, Nature Communications, 7, 1–9, https://doi.org/10.1038/ncomms13428, 2016.

1139   Keenan, T. F., Migliavacca, M., Papale, D., Baldocchi, D., Reichstein, M., Torn, M., and Wutzler, T.:
1140   Widespread inhibition of daytime ecosystem respiration, Nature Ecology and Evolution, 3, 407–415,
1141   https://doi.org/10.1038/s41559-019-0809-2, 2019.

1142   Keenan, T. F., Luo, X., Stocker, B. D., De Kauwe, M. G., Medlyn, B. E., Prentice, I. C., Smith, N.
1143   G., Terrer, C., Wang, H., Zhang, Y., and Zhou, S.: A constraint on historic growth in global
1144   photosynthesis due to rising CO2, Nat. Clim. Chang., 1–6, https://doi.org/10.1038/s41558-023-
1145   01867-2, 2023.

1146   Li, M., Cao, S., and Zhu, Z.: Spatiotemporally consistent global dataset of the GIMMS Normalized
1147   Difference Vegetation Index (PKU GIMMS NDVI) from 1982 to 2020, Earth System Science Data
1148   Discussions, 1–31, https://doi.org/10.5194/essd-2023-1, 2023.

1149   Liu, Y., Holtzman, N. M., and Konings, A. G.: Global ecosystem-scale plant hydraulic traits
1150   retrieved using model–data fusion, Hydrology and Earth System Sciences, 25, 2399–2417,
1151   https://doi.org/10.5194/hess-25-2399-2021, 2021.

1152   Luo, X., Zhou, H., Satriawan, T. W., Tian, J., Zhao, R., Keenan, T. F., Griffith, D. M., Sitch, S.,
1153   Smith, N. G., and Still, C. J.: Mapping the global distribution of C4 vegetation using observations
1154   and optimality theory, Nat Commun, 15, 1219, https://doi.org/10.1038/s41467-024-45606-3, 2024.

1155   Ma, H. and Liang, S.: Development of the GLASS 250-m leaf area index product (version 6) from
1156   MODIS data using the bidirectional LSTM deep learning model, Remote Sensing of Environment,
1157   273, 112985, https://doi.org/10.1016/j.rse.2022.112985, 2022.

1158   Ma, H., Zeng, J., Chen, N., Zhang, X., Cosh, M. H., and Wang, W.: Satellite surface soil moisture
1159   from SMAP, SMOS, AMSR2 and ESA CCI: A comprehensive assessment using global ground-
1160   based observations, Remote Sensing of Environment, 231, 111215,
1161   https://doi.org/10.1016/j.rse.2019.111215, 2019.

1162 Ma, Y., Zhang, Z., Kang, Y., and Özdoğan, M.: Corn yield prediction and uncertainty analysis based
1163 on remotely sensed variables using a Bayesian neural network approach, Remote Sensing of
1164 Environment, 259, 112408, https://doi.org/10.1016/j.rse.2021.112408, 2021.

1165 Myneni, R., Knyazikhin, Y., and Park, T.: MCD15A3H MODIS/Terra+Aqua Leaf Area
1166 Index/FPAR 4-day L4 Global 500m SIN Grid V006 [Data set], NASA EOSDIS Land Processes
1167 DAAC., https://doi.org/10.5067/MODIS/MCD15A3H.006, 2015a.

1168 Myneni, R., Knyazikhin, Y., and Park, T.: MOD15A2H MODIS/Terra Leaf Area Index/FPAR 8-
1169 Day L4 Global 500m SIN Grid V006 [Data set], NASA EOSDIS Land Processes DAAC,
1170 https://doi.org/10.5067/MODIS/MOD15A2H.006, 2015b.

1171 O'Sullivan, M., Spracklen, D. V., Batterman, S. A., Arnold, S. R., Gloor, M., and Buermann, W.:
1172 Have Synergies Between Nitrogen Deposition and Atmospheric CO 2 Driven the Recent
1173 Enhancement of the Terrestrial Carbon Sink?, Global Biogeochemical Cycles, 33, 163–180,
1174 https://doi.org/10.1029/2018GB005922, 2019.

1175 O'Sullivan, M., Smith, W. K., Sitch, S., Friedlingstein, P., Arora, V. K., Haverd, V., Jain, A. K., Kato,
1176 E., Kautz, M., Lombardozzi, D., Nabel, J. E. M. S., Tian, H., Vuichard, N., Wiltshire, A., Zhu, D.,
1177 and Buermann, W.: Climate-Driven Variability and Trends in Plant Productivity Over Recent
1178 Decades Based on Three Global Products, Global Biogeochemical Cycles, 34,
1179 https://doi.org/10.1029/2020GB006613, 2020.

1180 Pastorello, G., Trotta, C., Canfora, E., Chu, H., Christianson, D., Cheah, Y. W., Poindexter, C.,
1181 Chen, J., Elbashandy, A., Humphrey, M., Isaac, P., Polidori, D., Ribeca, A., van Ingen, C., Zhang, L.,
1182 Amiro, B., Ammann, C., Arain, M. A., Ardö, J., Arkebauer, T., Arndt, S. K., Arriga, N., Aubinet, M.,
1183 Aurela, M., Baldocchi, D., Barr, A., Beamesderfer, E., Marchesini, L. B., Bergeron, O., Beringer, J.,
1184 Bernhofer, C., Berveiller, D., Billesbach, D., Black, T. A., Blanken, P. D., Bohrer, G., Boike, J.,
1185 Bolstad, P. V., Bonal, D., Bonnefond, J. M., Bowling, D. R., Bracho, R., Brodeur, J., Brümmer, C.,
1186 Buchmann, N., Burban, B., Burns, S. P., Buysse, P., Cale, P., Cavagna, M., Cellier, P., Chen, S.,
1187 Chini, I., Christensen, T. R., Cleverly, J., Collalti, A., Consalvo, C., Cook, B. D., Cook, D., Coursolle,
1188 C., Cremonese, E., Curtis, P. S., D'Andrea, E., da Rocha, H., Dai, X., Davis, K. J., De Cinti, B., de
1189 Grandcourt, A., De Ligne, A., De Oliveira, R. C., Delpierre, N., Desai, A. R., Di Bella, C. M., di
1190 Tommasi, P., Dolman, H., Domingo, F., Dong, G., Dore, S., Duce, P., Dufrêne, E., Dunn, A.,
1191 Dušek, J., Eamus, D., Eichelmann, U., ElKhidir, H. A. M., Eugster, W., Ewenz, C. M., Ewers, B.,
1192 Famulari, D., Fares, S., Feigenwinter, I., Feitz, A., Fensholt, R., Filippa, G., Fischer, M., Frank, J.,
1193 Galvagno, M., Gharun, M., Gianelle, D., et al.: The FLUXNET2015 dataset and the ONEFlux
1194 processing pipeline for eddy covariance data, Scientific data, 7, 225,
1195 https://doi.org/10.1038/s41597-020-0534-3, 2020.

1196 Peñuelas, J., Ciais, P., Canadell, J. G., Janssens, I. A., Fernández-Martínez, M., Carnicer, J.,
1197 Obersteiner, M., Piao, S., Vautard, R., and Sardans, J.: Shifting from a fertilization-dominated to a
1198 warming-dominated period, Nature Ecology and Evolution, 1, 1438–1445,
1199 https://doi.org/10.1038/s41559-017-0274-8, 2017.

1200 Piao, S., Wang, X., Park, T., Chen, C., Lian, X., He, Y., Bjerke, J. W., Chen, A., Ciais, P.,
1201 Tømmervik, H., Nemani, R. R., and Myneni, R. B.: Characteristics, drivers and feedbacks of global

1202 greening, Nature Reviews Earth and Environment, 1, 14–27, https://doi.org/10.1038/s43017-019-
1203 0001-x, 2020.

1204 Prentice, I. C., Dong, N., Gleason, S. M., Maire, V., and Wright, I. J.: Balancing the costs of carbon
1205 gain and water transport: testing a new theoretical framework for plant functional ecology, Ecology
1206 Letters, 17, 82–91, https://doi.org/10.1111/ele.12211, 2014.

1207 Reich, P. B., Hobbie, S. E., and Lee, T. D.: Plant growth enhancement by elevated CO_2 eliminated
1208 by joint water and nitrogen limitation, Nature Geoscience, 7, 920–924,
1209 https://doi.org/10.1038/ngeo2284, 2014.

1210 Reichstein, M., Camps-Valls, G., Stevens, B., Jung, M., Denzler, J., Carvalhais, N., and Prabhat:
1211 Deep learning and process understanding for data-driven Earth system science, Nature, 566, 195–
1212 204, https://doi.org/10.1038/s41586-019-0912-1, 2019.

1213 Ruehr, S., Keenan, T. F., Williams, C., Zhou, Y., Lu, X., Bastos, A., Canadell, J. G., Prentice, I. C.,
1214 Sitch, S., and Terrer, C.: Evidence and attribution of the enhanced land carbon sink, Nat Rev Earth
1215 Environ, 1–17, https://doi.org/10.1038/s43017-023-00456-3, 2023.

1216 Running, S., Mu, Q., and Zhao, M.: MOD17A2H MODIS/Terra Gross Primary Productivity 8-Day
1217 L4 Global 500m SIN Grid V006, https://doi.org/10.5067/MODIS/MOD17A2H.006, 2015.

1218 Ryu, Y., Jiang, C., Kobayashi, H., and Detto, M.: MODIS-derived global land products of shortwave
1219 radiation and diffuse and total photosynthetically active radiation at 5 km resolution from 2000,
1220 Remote Sensing of Environment, 204, 812–825, https://doi.org/10.1016/j.rse.2017.09.021, 2018.

1221 Ryu, Y., Berry, J. A., and Baldocchi, D. D.: What is global photosynthesis? History, uncertainties and
1222 opportunities, Remote Sensing of Environment, 223, 95–114,
1223 https://doi.org/10.1016/j.rse.2019.01.016, 2019.

1224 Sabater, J. M.: ERA5-Land monthly averaged data from 1981 to present., Copernicus Climate
1225 Change Service (C3S) Climate Data Store (CDS), https://doi.org/doi:10.24381/cds.68d2bb30, 2019.

1226 Schaaf, C. and Wang, Z.: MCD43C4 MODIS/Terra+Aqua BRDF/Albedo Nadir BRDF-Adjusted
1227 Ref Daily L3 Global 0.05Deg CMG V006 [Data set], NASA EOSDIS Land Processes DAAC.,
1228 https://doi.org/10.5067/MODIS/MCD43C4.006, 2015.

1229 Schwalm, C. R., Anderegg, W. R. L., Michalak, A. M., Fisher, J. B., Biondi, F., Koch, G., Litvak, M.,
1230 Ogle, K., Shaw, J. D., Wolf, A., Huntzinger, D. N., Schaefer, K., Cook, R., Wei, Y., Fang, Y., Hayes,
1231 D., Huang, M., Jain, A., and Tian, H.: Global patterns of drought recovery, Nature, 548, 202–205,
1232 https://doi.org/10.1038/nature23021, 2017.

1233 Smith, W. K., Reed, S. C., Cleveland, C. C., Ballantyne, A. P., Anderegg, W. R. L., Wieder, W. R.,
1234 Liu, Y. Y., and Running, S. W.: Large divergence of satellite and Earth system model estimates of
1235 global terrestrial CO_2 fertilization, Nature Climate Change, 6, 306–310,
1236 https://doi.org/10.1038/nclimate2879, 2016.

1237 Ştefan, V. and Levin, S.: plotbiomes: R package for plotting Whittaker biomes with ggplot2, ,
1238 https://doi.org/10.5281/zenodo.7145245, 2018.

1239   Still, C. J., Berry, J. A., Collatz, G. J., and DeFries, R. S.: Global distribution of C3 and C4
1240   vegetation: Carbon cycle implications, Global Biogeochemical Cycles, 17,
1241   https://doi.org/10.1029/2001gb001807, 2003.

1242   Still, C. J., Berry, J. A., Collatz, G. J., and DeFries, R. S.: ISLSCP II C4 Vegetation Percentage, in:
1243   Hall, Forrest G., G. Collatz, B. Meeson, S. Los, E. Brown de Colstoun, and D. Landis (eds.).
1244   ISLSCP Initiative II Collection. Data set., http://dx.doi.org/10.3334/ORNLDAAC/932, 2009.

1245   Stocker, B. D., Zscheischler, J., Keenan, T. F., Prentice, I. C., Peñuelas, J., and Seneviratne, S. I.:
1246   Quantifying soil moisture impacts on light use efficiency across biomes, New Phytologist, 218,
1247   1430–1449, https://doi.org/10.1111/nph.15123, 2018.

1248   Stocker, B. D., Zscheischler, J., Keenan, T. F., Prentice, I. C., Seneviratne, S. I., and Peñuelas, J.:
1249   Drought impacts on terrestrial primary production underestimated by satellite monitoring, Nature
1250   Geoscience, 12, 264–270, https://doi.org/10.1038/s41561-019-0318-6, 2019.

1251   Stocker, B. D., Tumber-Dávila, S. J., Konings, A. G., Anderson, M. C., Hain, C., and Jackson, R. B.:
1252   Global patterns of water storage in the rooting zones of vegetation, Nat. Geosci., 16, 250–256,
1253   https://doi.org/10.1038/s41561-023-01125-2, 2023.

1254   Terrer, C., Jackson, R. B., Prentice, I. C., Keenan, T. F., Kaiser, C., Vicca, S., Fisher, J. B., Reich, P.
1255   B., Stocker, B. D., Hungate, B. A., Peñuelas, J., McCallum, I., Soudzilovskaia, N. A., Cernusak, L. A.,
1256   Talhelm, A. F., Van Sundert, K., Piao, S., Newton, P. C. D., Hovenden, M. J., Blumenthal, D. M.,
1257   Liu, Y. Y., Müller, C., Winter, K., Field, C. B., Viechtbauer, W., Van Lissa, C. J., Hoosbeek, M. R.,
1258   Watanabe, M., Koike, T., Leshyk, V. O., Polley, H. W., and Franklin, O.: Nitrogen and phosphorus
1259   constrain the CO2 fertilization of global plant biomass, Nature Climate Change, 9, 684–689,
1260   https://doi.org/10.1038/s41558-019-0545-2, 2019.

1261   Thoning, K. W., Crotwell, A. M., and Mund, J. W.: Atmospheric Carbon Dioxide Dry Air Mole
1262   Fractions from continuous measurements at Mauna Loa, Hawaii, Barrow, Alaska, American Samoa
1263   and South Pole. 1973-2020, Version 2021-08-09, National Oceanic and Atmospheric Administration
1264   (NOAA), Global Monitoring Laboratory (GML), Boulder, Colorado, USA,
1265   https://doi.org/10.15138/yaf1-bk21, 2021.

1266   Tramontana, G., Ichii, K., Camps-Valls, G., Tomelleri, E., and Papale, D.: Uncertainty analysis of
1267   gross primary production upscaling using Random Forests, remote sensing and eddy covariance
1268   data, Remote Sensing of Environment, 168, 360–373, https://doi.org/10.1016/j.rse.2015.07.015,
1269   2015.

1270   Tramontana, G., Jung, M., Schwalm, C. R., Ichii, K., Camps-Valls, G., Ráduly, B., Reichstein, M.,
1271   Arain, M. A., Cescatti, A., Kiely, G., Merbold, L., Serrano-Ortiz, P., Sickert, S., Wolf, S., and Papale,
1272   D.: Predicting carbon dioxide and energy fluxes across global FLUXNET sites with regression
1273   algorithms, Biogeosciences, 13, 4291–4313, https://doi.org/10.5194/bg-13-4291-2016, 2016.

1274   Ueyama, M., Ichii, K., Kobayashi, H., Kumagai, T., Beringer, J., Merbold, L., Euskirchen, E. S.,
1275   Hirano, T., Marchesini, L. B., Baldocchi, D., Saitoh, T. M., Mizoguchi, Y., Ono, K., Kim, J.,
1276   Varlagin, A., Kang, M., Shimizu, T., Kosugi, Y., Bret-Harte, M. S., Machimura, T., Matsuura, Y.,
1277   Ohta, T., Takagi, K., Takanashi, S., and Yasuda, Y.: Inferring CO2 fertilization effect based on

1278　global monitoring land-atmosphere exchange with a theoretical model, Environmental Research
1279　Letters, 15, 84009, https://doi.org/10.1088/1748-9326/ab79e5, 2020.

1280　Villarreal, S. and Vargas, R.: Representativeness of FLUXNET Sites Across Latin America, Journal
1281　of Geophysical Research: Biogeosciences, 126, e2020JG006090,
1282　https://doi.org/10.1029/2020JG006090, 2021.

1283　Walker, A. P., De Kauwe, M. G., Bastos, A., Belmecheri, S., Georgiou, K., Keeling, R. F.,
1284　McMahon, S. M., Medlyn, B. E., Moore, D. J. P., Norby, R. J., Zaehle, S., Anderson-Teixeira, K. J.,
1285　Battipaglia, G., Brienen, R. J. W., Cabugao, K. G., Cailleret, M., Campbell, E., Canadell, J. G., Ciais,
1286　P., Craig, M. E., Ellsworth, D. S., Farquhar, G. D., Fatichi, S., Fisher, J. B., Frank, D. C., Graven, H.,
1287　Gu, L., Haverd, V., Heilman, K., Heimann, M., Hungate, B. A., Iversen, C. M., Joos, F., Jiang, M.,
1288　Keenan, T. F., Knauer, J., Körner, C., Leshyk, V. O., Leuzinger, S., Liu, Y., MacBean, N., Malhi, Y.,
1289　McVicar, T. R., Penuelas, J., Pongratz, J., Powell, A. S., Riutta, T., Sabot, M. E. B., Schleucher, J.,
1290　Sitch, S., Smith, W. K., Sulman, B., Taylor, B., Terrer, C., Torn, M. S., Treseder, K. K., Trugman, A.
1291　T., Trumbore, S. E., van Mantgem, P. J., Voelker, S. L., Whelan, M. E., and Zuidema, P. A.:
1292　Integrating the evidence for a terrestrial carbon sink caused by increasing atmospheric CO_2, New
1293　Phytologist, 229, 2413–2445, https://doi.org/10.1111/nph.16866, 2021.

1294　Walther, S., Besnard, S., Nelson, J. A., El-Madany, T. S., Migliavacca, M., Weber, U., Carvalhais, N.,
1295　Ermida, S. L., Brümmer, C., Schrader, F., Prokushkin, A. S., Panov, A. V., and Jung, M.: Technical
1296　note: A view from space on global flux towers by MODIS and Landsat: the FluxnetEO data set,
1297　Biogeosciences, 19, 2805–2840, https://doi.org/10.5194/bg-19-2805-2022, 2022.

1298　Wan, Z., Hook, S., and Hulley, G.: MOD11A1 MODIS/Terra Land Surface
1299　Temperature/Emissivity Daily L3 Global 1km SIN Grid V006 [Data set], NASA EOSDIS Land
1300　Processes DAAC, https://doi.org/10.5067/MODIS/MOD11A1.006, 2015a.

1301　Wan, Z., Hook, S., and Hulley, G.: MYD11A1 MODIS/Aqua Land Surface
1302　Temperature/Emissivity Daily L3 Global 1km SIN Grid V006 [Data set], NASA EOSDIS Land
1303　Processes DAAC, https://doi.org/10.5067/MODIS/MYD11A1.006, 2015b.

1304　Wang, H., Prentice, I. C., Keenan, T. F., Davis, T. W., Wright, I. J., Cornwell, W. K., Evans, B. J.,
1305　and Peng, C.: Towards a universal model for carbon dioxide uptake by plants, Nature Plants, 3, 734–
1306　741, https://doi.org/10.1038/s41477-017-0006-8, 2017.

1307　Warm Winter 2020 Team: Warm Winter 2020 ecosystem eddy covariance flux product for 73
1308　stations in FLUXNET-Archive format—release 2022-1 (Version 1.0),
1309　https://doi.org/10.18160/2G60-ZHAK, 2022.

1310　Wenzel, S., Cox, P. M., Eyring, V., and Friedlingstein, P.: Projected land photosynthesis constrained
1311　by changes in the seasonal cycle of atmospheric CO_2, Nature, 538, 499–501,
1312　https://doi.org/10.1038/nature19772, 2016.

1313　Xiao, J., Zhuang, Q., Baldocchi, D. D., Law, B. E., Richardson, A. D., Chen, J., Oren, R., Starr, G.,
1314　Noormets, A., Ma, S., Verma, S. B., Wharton, S., Wofsy, S. C., Bolstad, P. V., Burns, S. P., Cook, D.
1315　R., Curtis, P. S., Drake, B. G., Falk, M., Fischer, M. L., Foster, D. R., Gu, L., Hadley, J. L., Hollinger,
1316　D. Y., Katul, G. G., Litvak, M., Martin, T. A., Matamala, R., McNulty, S., Meyers, T. P., Monson, R.
1317　K., Munger, J. W., Oechel, W. C., Paw U, K. T., Schmid, H. P., Scott, R. L., Sun, G., Suyker, A. E.,

and Torn, M. S.: Estimation of net ecosystem carbon exchange for the conterminous United States by combining MODIS and AmeriFlux data, Agricultural and Forest Meteorology, 148, 1827–1847, https://doi.org/10.1016/j.agrformet.2008.06.015, 2008.

Xie, X., Chen, J. M., Yuan, W., Guan, X., Jin, H., and Leng, J.: A Practical Algorithm for Correcting Topographical Effects on Global GPP Products, Journal of Geophysical Research: Biogeosciences, 128, e2023JG007553, https://doi.org/10.1029/2023JG007553, 2023.

Xie, Y., Gibbs, H. K., and Lark, T. J.: Landsat-based Irrigation Dataset (LANID): 30m resolution maps of irrigation distribution, frequency, and change for the US, 1997–2017, Earth System Science Data, 13, 5689–5710, https://doi.org/10.5194/essd-13-5689-2021, 2021.

Yan, K., Park, T., Yan, G., Chen, C., Yang, B., Liu, Z., Nemani, R. R., Knyazikhin, Y., and Myneni, R. B.: Evaluation of MODIS LAI/FPAR product collection 6. Part 1: Consistency and improvements, Remote Sensing, 8, 1–16, https://doi.org/10.3390/rs8050359, 2016a.

Yan, K., Park, T., Yan, G., Liu, Z., Yang, B., Chen, C., Nemani, R. R., Knyazikhin, Y., and Myneni, R. B.: Evaluation of MODIS LAI/FPAR product collection 6. Part 2: Validation and intercomparison, Remote Sensing, 8, 460, https://doi.org/10.3390/rs8060460, 2016b.

Yang, F., Ichii, K., White, M. A., Hashimoto, H., Michaelis, A. R., Votava, P., Zhu, A. X., Huete, A., Running, S. W., and Nemani, R. R.: Developing a continental-scale measure of gross primary production by combining MODIS and AmeriFlux data through Support Vector Machine approach, Remote Sensing of Environment, 110, 109–122, https://doi.org/10.1016/j.rse.2007.02.016, 2007.

Yang, R., Wang, J., Zeng, N., Sitch, S., Tang, W., McGrath, M. J., Cai, Q., Liu, D., Lombardozzi, D., Tian, H., Jain, A. K., and Han, P.: Divergent historical GPP trends among state-of-the-art multi-model simulations and satellite-based products, Earth System Dynamics, 13, 833–849, https://doi.org/10.5194/esd-13-833-2022, 2022.

Yuan, H., Dai, Y., Xiao, Z., Ji, D., and Shangguan, W.: Reprocessing the MODIS Leaf Area Index products for land surface and climate modelling, Remote Sensing of Environment, 115, 1171–1187, https://doi.org/10.1016/j.rse.2011.01.001, 2011.

Zeng, J., Matsunaga, T., Tan, Z.-H., Saigusa, N., Shirai, T., Tang, Y., Peng, S., and Fukuda, Y.: Global terrestrial carbon fluxes of 1999–2019 estimated by upscaling eddy covariance data with a random forest, Sci Data, 7, 313, https://doi.org/10.1038/s41597-020-00653-5, 2020.

Zeng, N., Zhao, F., Collatz, G. J., Kalnay, E., Salawitch, R. J., West, T. O., and Guanter, L.: Agricultural Green Revolution as a driver of increasing atmospheric CO2 seasonal amplitude, Nature, 515, 394–397, https://doi.org/10.1038/nature13893, 2014.

Zhang, Y.: A global spatially contiguous solar-induced fluorescence (CSIF) dataset using neural networks (2000-2020), National Tibetan Plateau Data Center, https://doi.org/10.11888/Ecolo.tpdc.271751., 2021.

Zhang, Y., Joiner, J., Hamed Alemohammad, S., Zhou, S., and Gentine, P.: A global spatially contiguous solar-induced fluorescence (CSIF) dataset using neural networks, Biogeosciences, 15, 5779–5800, https://doi.org/10.5194/bg-15-5779-2018, 2018.

1356   Zheng, Y., Shen, R., Wang, Y., Li, X., Liu, S., Liang, S., Chen, J. M., Ju, W., Zhang, L., and Yuan,
1357   W.: Improved estimate of global gross primary production for reproducing its long-Term variation,
1358   1982-2017, Earth System Science Data, 12, 2725–2746, https://doi.org/10.5194/essd-12-2725-
1359   2020, 2020.

1360   Zhu, Z., Piao, S., Myneni, R. B., Huang, M., Zeng, Z., Canadell, J. G., Ciais, P., Sitch, S.,
1361   Friedlingstein, P., Arneth, A., Cao, C., Cheng, L., Kato, E., Koven, C., Li, Y., Lian, X., Liu, Y., Liu,
1362   R., Mao, J., Pan, Y., Peng, S., Peuelas, J., Poulter, B., Pugh, T. A. M., Stocker, B. D., Viovy, N.,
1363   Wang, X., Wang, Y., Xiao, Z., Yang, H., Zaehle, S., and Zeng, N.: Greening of the Earth and its
1364   drivers, Nature Climate Change, 6, 791–795, https://doi.org/10.1038/nclimate3004, 2016.

1365